Laser-Induced Plasma Spectroscopy on steel induced by low energy nanosecond pulses

Spectroscopie par claquage laser de l'acier avec un faisceau nano-pulsé à faible énergie

A Thesis Submitted to the Division of Graduate Studies of the Royal Military College of Canada
by

Kevin M. N. Woodcock

In Partial Fulfillment of the Requirements of the Degree of Master of Science in Physics

September, 2022

Abstract

This Master's work was completed to determine the viability of measuring the chemical matrix of an unknown inorganic sample by laser-induced plasma spectroscopy (LIPS) without using a Q-switch time delay gate for data acquisition. The commonly used calibration-free laser-induced breakdown spectroscopy (LIBS) method is unreliable for long distance remote sensing applications due to atmospheric thermal blooming along the laser beam path. The calibrated LIBS technique can be modified to accurately measure non-trace chemical matrices of inorganic material over long distances without using a Q-switch time delay mechanism.

Five stainless steel and four carbon steel samples with known elemental compositions were selected for analysis. A nano-pulse laser with an 80 μm beam waist diameter generated a plasma on the sample surface and a Horiba iHR-320 spectrometer captured spectra of the generated plasma at the surface of each sample. Boltzmann plots were created for each sample using a set of spectral lines to demonstrate a partial local thermodynamic equilibrium (pLTE) in the plasma. Both the Fe I and Cr I species demonstrated necessary properties of LTE by satisfying the McWhirter and Hey criterion for threshold electron density and by having a linear Boltzmann relationship. From the Boltzmann plots, the Fe I species reached 6000 K and the Cr I species reached 3500 K in each sample. It was not possible to confirm that all temperatures converged to a single value without using a Q-switch to create a time delay. The electron density within the plasma was between 6.8 and 8.4×10^{16} cm^{-3} for all samples. Amplitudes of the spectral lines for Cr I at 520.84 nm and Fe I at 526.91 nm followed a linear relationship with the elemental concentrations for the steels given by the manufacturer. This Calibrated LIPS technique which operated without a Q-switch gating mechanism can be used to determine the elemental matrix of inorganic materials at a distance where thermal blooming renders a LIBS experiment unreliable.

Résumé

Ce travail de recherche vise à déterminer la faisabilité de la présence du contenu chimique dans un matériau inorganique à l'aide de la spectroscopie par claquage-laser sans créer de délai entre le q-commutateur et la récolte de données. La présente méthode de la spectroscopie par claquage laser appliquée avec délai n'est pas réaliste à longue portée lors d'un exercice par télédétection à cause des effets thermiques de l'atmosphère qui perturbent le faisceau laser. La technique de la spectroscopie par claquage-laser à longue portée doit donc être modifiée afin de déceler la teneur chimique d'un matériau inorganique sans faire appel à un délai entre la q-commutation et la récolte de données.

Cinq (5) aciers inoxydables et quatre (4) autres de fonte avec des teneurs chimiques connues furent analysées. Un laser nano-pulsé ayant une taille de faisceau égale à 80 μm créait un plasma à la surface des matériaux choisis pour cette étude. Un spectromètre Horiba iHR-320 faisait une saisie rapide d'un spectre en longueur d'onde à une distance de l'ordre de 50 mm des échantillons. En outre, des courbes de Boltzmann ont été obtenues à partir des raies spectroscopiques provenant des spectres de chaque matériau afin de démontrer qu'il existait un équilibre thermodynamique partiel dans le plasma. Les deux atomes ionisés une fois du fer Fe I et du chrome Cr I démontrent que l'équilibre thermodynamique local est au moins partiellement satisfait. De plus, selon les critères de McWhirter et Hey, le seuil de la densité électronique et la linéarisation de la courbe de Boltzmann nous indique aussi qu'un équilibre thermodynamique est partiellement satisfait. D'après les courbes d'activation basées sur la statistique de Maxwell-Boltzmann, les températures des ions de Fe I et Cr I furent estimées à 6000 K et 3500 K, respectivement. Cependant, il n'a pas été possible de confirmer que les températures estimées tendent vers une valeur constante en se livrant à des analyses en variant les temps de délai entre la q-commutation et la récolte de données. Les densités électroniques obtenues pour les échantillons

lors de la formation du plasma variaient entre 6.8×10^{16} cm^{-3} et 8.4×10^{16} cm^{-3}. Les amplitudes des raies du chrome Cr I à 520.84 nm et du fer Fe I à 526.91 nm variaient linéairement en fonction des teneurs chimiques indiquées par le fournisseur. Cette méthode de spectroscopie par claquage-laser calibrée, en l'absence du délai, démontre qu'il est possible de déterminer les teneurs dans l'acier lors d'une saisie à longue portée, qui est souvent perturbée par des effets parasites thermiques.

Contents

List of Tables

List of Figures

Acronyms

AAS Atomic Absorption Spectroscopy. 1

CF-LIBS Calibration-Free Laser Induced Breakdown Spectroscopy. 19

CS Carbon Steel. 22

ICP/OES Inductively Coupled Plasma/Optical Emission Spectroscopy. 1

LIBS Laser Induced Breakdown Spectroscopy. 1

LIP Laser-Induced Plasma. 4

LIPS Laser Induced Plasma Spectroscopy. 3

LOD Limit Of Detection. 52

MPI Multiphoton Ionization. 7

OAP Off-Axis Parabolic Mirror. 40

PC Pockels Cell. 35

pLTE Partial Local Thermodynamic Equilibrium. 4

SEM Scanning Electron Microscope. 64

SESAM Semiconductor Saturable Absorber Material. 35

SS Stainless Steel. 22

1 Introduction

Interest in the detection of heavy metals in organic and inorganic materials has been growing over the past couple of decades due to their hazardous nature to humans [1]. Research on water and soil samples have been conducted to find trace amounts of heavy metals from anthropogenic sources with the goal of mapping pollution [2, 3]. The farming industry has interest in determining heavy metal concentration in soil and foods, such as potatoes, to confirm safe consumption for humans [4, 5]. Manufacturers in metals and plastics have an interest in quick methods to determine product quality control [6, 7]. There is a need to develop spectroscopic techniques to evaluate the chemical matrices of organic and inorganic materials.

Historically, techniques such as Inductively Coupled Plasma/Optical Emission Spectroscopy (ICP/OES) and Atomic Absorption Spectroscopy (AAS) have been used to determine the concentration of trace elements in organic and inorganic materials. The ICP/OES and AAS methods are costly, bulky and usually require tedious preparation before analysis [4]. The emergence of Laser Induced Breakdown Spectroscopy (LIBS) is especially useful as a cheap, quick, and potentially portable replacement for ICP/OES and AAS in atomic concentration determination. LIBS provides the opportunity for remotely sensing the atomic concentration of a sample, whereas ICP/OES and AAS require a sample to be extracted, prepared and supplied into the analysis chambers.

LIBS has developed at a very fast pace during the past ten years. The energy per pulse required for breakdown is typically within 10 mJ to 100 mJ or more to produce a plasma that is hot enough to ionize a large concentration of electrons of about (10^{17} cm^{-3}). A nanopulse laser within the 10 mJ - 100 mJ range can be easily focused to a small spot on a sample producing a power density greater than 1 GW cm^{-2}. At

this irradiance, bound electrons are removed from their parent atoms, leaving behind a plasma that consists of a gas of electrons and ionized atoms. As the plasma cools, the parent atoms emit photons when electrons de-excite to lower energy levels during a collision with another atom. A spectrometer can be gated to create a time-delay between the lasing nanopulse and data acquisition in order to measure the atomic de-excitation during the plasma cooling stage. It has been shown that the temperature of the plasma gas and ions reaches an equilibrium within a few nanoseconds to a few microseconds when the plasma cools down. The spectroscopic signal during the hot plasma expansion is noisy and difficult to analyze. During expansion, the plasma temperature keeps increasing and the plasma is not in thermodynamic equilibrium.

The nanosecond laser used in this thesis work delivered 0.5 mJ pulses at a 2000 Hz repetition rate. A pulse delay generator was not used to delay the start of the data acquisition with respect to the lasing nanosecond pulse. No delay was used in this investigation because it is not always practical in remote sensing applications to trigger the laser Q-switch with a camera. Some sudden turbulence in the atmosphere (wind, dust) could cause delays that are difficult to predict during a real-time data acquisition [8]. Adaptive optics can handle these situations, though setups can be bulky and complex. In this thesis, steel samples were irradiated using low energy nanosecond pulses at a high repetition rate. The low energy pulses were focused to produce a sufficiently high irradiance to induce breakdown at the surface of the steel samples. The focused laser was able to ionize the air at the focal point of the laser. It was possible to see sparking produce a bluish glow and one could hear sizzling while the laser was irradiating the metal surface. Shallow holes were drilled at the metal surface by the laser irradiance. It was concluded that the ablated matter (containing atomic species such as Fe and Cr) was ejected from the surface within the plume.

A description of the experimental setup will be given in Chapter 2. An analysis of the spectroscopic results will be presented in Chapter 3 to show that Laser-Induced Plasma Spectroscopy (LIPS), a modified technique of LIBS, is a viable spectroscopic technique for long distance imaging.

It was shown that various spectroscopic peaks could be identified on Stainless Steel 304 (SS304) and 316 (SS316). Instead of creating a delay, all spectra were integrated over a time period much longer than the laser repetition rate. Many cycles of plasma formation passed within a single integration block. During the investigation, many spectrograms were taken repetitively for a given sample and it was observed that the spectroscopic peaks in the spectrograms reached a maximum before decreasing with time. A time series of spectrograms reached a maximum amplitude after 3 integration blocks, then the amplitudes of each spectrogram decreased slowly over time. As the changes in the peaks varied slowly, we concluded that an equilibrium was reached during the surface heating process. It is possible that the peaks of a spectroscopic time series decreased due to rust formation on the sample surface which obstructed the flow of free atoms (such as Fe and Cr) used to sustain the plasma.

1.0.1 Goal of this thesis

The primary objective of this thesis is to contribute to the ongoing demonstration of LIPS as a useful technique for remotely sensing elements in materials and to probe the method's effectiveness without using a Q-switch gating mechanism. As LIBS involves high energy laser pulses, it becomes less practical at large distances because atmospheric perturbations can cause thermal blooming, which could distort the laser beam. Therefore, a study involving LIPS without setting any time delay is more suitable to detect the presence of the non-trace elements and impurities in steel remotely. A set

of stainless steel (SS) and carbon steel (CS) samples were obtained to measure the concentration of chromium (Cr) and iron (Fe) and to characterize the resultant plasma by using the LIPS technique.

1.0.2 Structure of the manuscript

The spectroscopic methods mentioned earlier (ICP/OES and AAS) will be discussed in Sections 1.1. and 1.2, respectively. Section 1.3 will provide an in-depth description of Laser Induced Breakdown Spectroscopy in both inorganic and organic samples. The requirements and determination of partial Local Thermodynamic Equilibrium (pLTE) will be discussed in Section 1.4 as an initial condition required for a laser-induced plasma to form. Section 1.5 will detail different emission broadening mechanisms present in a hot plasma. Finally, the common quantitative analytical procedures for analysing LIBS spectrograms will be explained in Section 1.6.

Chapter 2 will focus on the experimental process. Section 2.1 will describe the structure and components of the experimental setup. Sections 2.2 and 2.3 will quantify the structure of the laser beam and detail the path the beam follows. Sections 2.4 and 2.5 will discuss parameters of the laser used in this experiment. Section 2.6 will outline the methodology and main differences between LIBS and LIPS. Section 2.7 will discuss components of the spectrometer and how the spectrograms were recorded.

Chapter 3 will detail the spectroscopic results of the experiment. Section 3.1 will give an overview of the analysis and how the spectroscopic line amplitudes were resolved. Section 3.2 will discuss self absorption in the chromium lines, and Section 3.3 will determine that the LIP is in pLTE and calculate the temperature and electron density of the LIP.

1.1 Inductively Coupled Plasma Optical Emission Spectroscopy

Inductively Coupled Plasma/Optical Emission Spectroscopy (ICP/OES) uses an RF generator (700W-1500W) to produce a strong AC magnetic field which accelerates electrons and atoms at a rate on the order of 40 MHz [9]. Neutral gas, such as Argon, is typically used to sustain the plasma. A tesla coil supplies the RF alternating current which vibrates the neutral gas molecules, atomizing (breaking the molecular bond) and ionizing them through collisions and heating the plasma on the order of 10000 K. Over a short period of time, the electrons and ions collide with new, neutral gas molecules to atomize and ionize the atoms in a chain reaction that sustains the plasma. The sample to be analyzed is converted to an aerosol in a nebulizer, then supplied into the plasma to be ionized. The plasma remains active at a temperature relative to the RF amplitude and as long as the RF power is supplied. Ions that move away from the Initial Radiation Zone (where plasma formation occurs) cool and recombine with free electrons, emitting a photon with a very specific energy and wavelength. Note that the same cooling mechanism occurs when a nanopulsed laser beam irradiates a metal surface. A spectrometer then captures the photons, recording the number of photons and their energy.

The main advantage of using ICP/OES is the reproducible, low-noise, high temperature plasma that is produced. ICP/OES produces a 6000+ K temperature plasma in the Initial Radiation Zone where sample ionization takes place. Some disadvantages of using ICP/OES include the preparation required prior to analysis, the low yield rate of nebulization and electrothermal vaporization, and ICP/OES is limited to laboratory research [9].

1.2 Atomic Absorption Spectroscopy

Atomic Absorption Spectroscopy (AAS) is a technique typically used when chemical composition of a sample is known but the chemical concentration is not. AAS is used to find the number density of a single species within a sample by measuring the laser intensity difference across the sample. A cathode lamp produces broadband emission and a monochromator selects light resonant with the ground state of the target element. The Beer-Lambert law dictates absorptance, α, through a medium as

$$\alpha = \epsilon \ell c \tag{1}$$

where ϵ (M^{-1} cm^{-1}) represents absorptivity of the species, ℓ (cm) is the optical path length of the medium, and c (M) is the chemical concentration of the species, where M is the molar concentration of the sample [10]. The rate that light is absorbed in media is shown by Equation 2.

$$\frac{dI(x)}{dx} = -\alpha \times I(x) \tag{2}$$

AAS is a simple but limited spectroscopic analysis tool. AAS tends to be a bulky setup and is currently limited to laboratories, but AAS does not typically require much sample preparation.

1.3 LASER Induced Breakdown Spectroscopy

1.3.1 LIBS on Crystalline Structures

Laser Induced Breakdown Spectroscopy (LIBS) in the air was first discovered in 1963 with the invention of Q-switched pulse lasers [11]. Initially, CCDs (charge-coupled devices) could only capture light over a small spectral window, limiting the applica-

tions of LIBS to homogeneous materials. The development of the ICCD (intensified charge-coupled device) in the 80s allowed for more accurate spectral readings over a broad wavelength window, increasing accessibility and interest in LIBS systems [12].

Early experiments were intended to begin understanding the fundamentals of laser induced breakdown. Three non-radioactive mechanisms cause ablation from the surface of a solid: photothermal, photochemical, and photophysical [13]. Photothermal ablation is the process of melting and evaporation from a material's surface due to heating from light absorption. This is the mechanism that took place when the metal samples were ablated in this investigation. Photochemical ablation is a non-thermal reaction. Electron excitation is linked to vibrational excitation in molecules [13]. Sufficiently strong photons or multi-photon impacts cause the vibrational energy to exceed molecular bonds, causing ejection of the molecule. Photophysical ablation is when both photothermal and photochemical ablation processes occur in a sample. Once material has been ablated, three main mechanisms induce ionization to produce to a laser induced plasma. The mechanisms are due to free electron-atom impact ionization, multiphoton ionization (MPI), and thermal ionization [12]. First, free electrons can absorb photons through inverse Bremsstrahlung absorption and collide with free atoms or ions in a gas [12]. With sufficient energy, an electron can impact a free atom or ion and eject another electron.

$$M + e^- -> M^+ + 2e^-$$

This reaction accelerates with time as newly ionized electrons absorb light to continue the cascade of free-free ionization. Another mechanism for electron generation in a plasma, MPI, is the simultaneous absorption of multiple photons to ionize an atom.

$$M + nh\nu -> M^{+} + e^{-}$$

The combined energy of n photons, $nh\nu$, must be greater than the band gap energy of the bound electron, otherwise known as the ionization potential ϵ_I. This mechanism is more likely to occur when using high energy photons and impacting a material with a low ionization potential ϵ_I. The third mechanism to initiate ionization occurs in a bulk absorbing material and is called "thermionic runaway". The increasing temperature on the surface of the material can ionize surface atoms to emit an electron. The electrons from the metal surface immediately recombine with the metal and are not impacted by the laser, however vapour molecules above the surface of the metal heat and emit free electrons [11]. These electrons absorb photons and begin the free-free absorption and collision cascade to produce a plasma. As the target's surface heats, the material melts and evaporates to feed the plasma. Plume expansion begins around 100 ps after first contact of the laser [12].

1.3.2 LIBS on Organic Materials

Laser absorption acts similarly in organics as it does in metals, though less work has been published on LIBS in organics because the molecular complexity of organic compounds makes spectra difficult to analyze. Photochemical ablation is the common mechanism to produce a plasma in organic compounds. Photon absorption excites an electron, which is coupled to the vibrational energy state of the organic molecule. Non-radiative processes, such as vibrations, heat adjacent molecules in a chain reaction to decrease the excited energy state over the timescale of 1 ps. On the timescale of 1 ns, a photon is emitted to relax the excited state of the molecule to an excited ground state. Non-radiative processes then de-excite a molecular state to the minimum ground state

[13].

Various processes exist that induce particle ablation in molecular solids from a laser. Single photon ionization can occur when the photon energy is greater than the molecular bond energy, causing dissociation. Multi-photon absorption can raise the vibrational energy state to dissociate the molecule. Multiple instantaneous photon absorptions can sum to excite the molecule beyond dissociation, called coherent multi-photon absorption. Multiple photons absorbed at different times can excite the molecule through multiple sequential energy states to dissociate the molecule, called incoherent multi-photon absorption. Ablation in organics results from a combination of photothermal and photochemical ablation, known as photophysical ablation [12, 13].

Some challenges exist when using LIBS to determine chemical concentration in organic matter such as food [14]. Foods have non-homogeneous matrices that are typically made up of complex molecules such as carbohydrates, fats, and proteins [4, 15]. LIBS on organic materials can lead to molecular fragments forming in the plasma. Molecules can be produced by ions in the plasma interacting with gases in the atmosphere or by the target evaporated by photochemical ablation. Due to the non-homogeneous and variable structure of food (even within a single sample), each lased spot reacts differently to the laser. Many trials of a sample are required to achieve reproducible results. It is also possible to perform LIBS on liquid foods, though the laser can produce splashing and ripples along the surface on contact which moves the sample away from the focal point, leading to shorter plasma lifetimes. Liquids can be frozen by lowering the internal temperature of the sample to resolve these problems without changing the chemical composition of the sample [16].

The high diversity of elements found in most foods leads to an issue of re-absorption

in the plasma due to both cold atoms at the plasma boundary and overlapping emission/absorption lines between different elements [4]. Re-absorption can typically be seen by a dip at the peak of emission lines due to the Stark effect broadening emission lines in a plasma. Re-absorption occurs at a higher rate as elemental concentration in a sample increases. Therefore, it is also possible to see this effect in a non-linear correlation between emission intensity and elemental concentration.

1.4 Thermodynamic Equilibrium in the Plasma

The McWhirter and Hey criteria requires that collisional excitation events across all population levels of an atom are predominant compared to its radiative de-excitation events [17, 18]. Energy loss is then considered sufficiently small compared to the energy transfer sustaining the plasma. Two more criteria must be satisfied for an expanding plasma. First, the relaxation time of the plasma must be much greater than the ionization time of the neutral atoms. This is seen by both the temperature and number density of the electrons sustaining over a longer time period than the formation period. For example, if the number density of electrons falls faster than electrons can be ionized through collisions or photon absorption, then the plasma will not sustain. Secondly, a plasma must not expand too quickly relative to the time between electron collisions. The diffusion length of an excited ion must be shorter than the variation of temperature and electron density in the plasma [19]. This means that temperature and electron density are homogeneous over a volume well beyond the local environment of an ion or atom. The McWhirter and Hey criteria are necessary for LTE to exist in a plasma, but they are not sufficient to claim that a given a plasma is in LTE [20]. The plasma must be locally described by a single temperature to obtain an LTE designation. In LTE, the center of the plasma lobe is uniform and the edges of the lobe are

more turbulent and less uniform.

It has been shown that within a few picoseconds during initial plasma expansion from laser irradiance, the plasma is not in LTE. After a few hundred picoseconds, electron collisions are the dominant process sustaining the plasma as it enters LTE. The plasma then begins to slowly cool through atomic collisional de-excitation and photon emission after a few microseconds.

1.5 Spectral Line Broadening Effects

1.5.1 Natural Line Broadening

The quantum mechanical uncertainty causes an energy spread of a given level within its finite lifetime. The energy spread ΔE is measured using the Heisenberg uncertainty principle

$$\Delta E \Delta t \geq \hbar \tag{3}$$

where ΔE corresponds to the linewidth and Δt is the transition lifetime. Nucleic and atomic transition lifetimes Δt are typically on the order of 10^{-24} s and 10^{-8} s, respectively [21]. Wave functions can be used to describe the state associated with a particle, such as an electron, as follows

$$\Psi(t) = \int_{-\infty}^{\infty} A_\omega e^{-i\omega t} d\omega = \int_{-\infty}^{\infty} A_E e^{-iEt/\hbar} dE \tag{4}$$

where

$$A_\omega = \int_{-\infty}^{\infty} \psi(t) e^{i\omega t} dt \,, \qquad A_E = \int_{-\infty}^{\infty} \psi(t) e^{iEt/\hbar} dt \tag{5}$$

Essentially, A_ω and A_E are Fourier transforms which carry a statistical weight for the amplitude of a periodic function at a given frequency. After integrating the amplitude A_ω (or A_E) times the periodic function of frequency ω, we obtain $\Psi(t)$, which is often referred to as the wavepacket of the particle. The wavepacket represents the localized waveform of the particle.

The number of particles that decay ΔN over a time Δt is proportional to the number of particles that exist in a given state, $N(t)$. This may be expressed as:

$$\Delta N = -\gamma N(t)\Delta t \tag{6}$$

where γ is the probability of the particle decaying per unit time and is the reciprocal of the mean lifetime [21]. In the context of electron decay, this would be seen as photon emission as the electron de-excites to a lower energy level. The number of particles in a given state would decay exponentially as

$$N(t) = N_0 e^{-\gamma t} \tag{7}$$

The average, or expected, number of particles in a single state $< N(t) >$ can be expressed through a probability function

$$< N(t) >= P(t)N_0 \tag{8}$$

where $P(t) = P_0 e^{-\gamma t}$. Values for γ are typically in the range of 10^8 s^{-1} [21]. The probability of finding a state within some space dx is given by $\int_x^{x+dx} |\Psi|^2 dx$, so we may say that the probability of a state existing after a given time is given by $\int_t^{t+dt} |\Psi|^2 dt$. This means that $|\Psi| \sim e^{-\gamma t/2}$ for $t \geq 0$.

The state of the electron is not stationary under a perturbation such as a periodically

varying electric field E. As a result, ψ may be cast as

$$\psi(t) \sim e^{-\gamma t/2} e^{-iE_0 t/\hbar} \tag{9}$$

where $e^{-iE_0 t/\hbar}$ is a phase factor related to the background electric field. The energy E_0 is the center energy of the electron within the electron band such as the one shown in Figure 1.

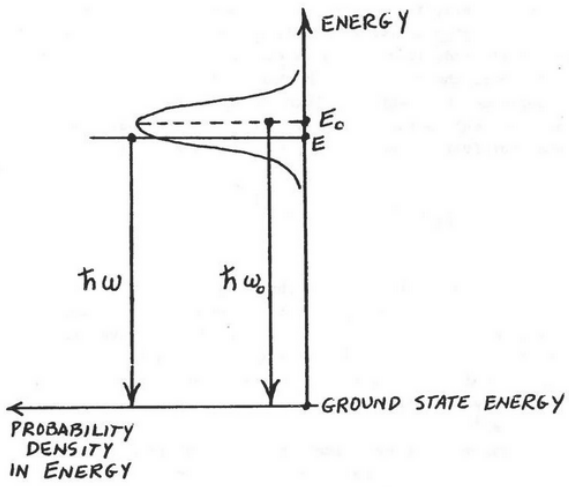

Figure 1: There is a quantum mechanical uncertainty in the emission energy from de-excitation events. Transitions from an excited state have a narrow band of possible de-excitation energies due to the Heisenberg uncertainty principle. Reprinted from [21].

As $\psi(t) \sim e^{-\gamma t/2}\, e^{-iE_0 t/\hbar}$ for all time $t \geq 0$, we can now apply the Fourier transform A_E introduced earlier as

$$A_E = \int_0^\infty A_0 e^{-\gamma t/2} e^{-iE_0 t/\hbar} e^{iEt/\hbar} dt \tag{10}$$

where A_0 is a normalization constant. After integration, we find that

$$A_E = \frac{A_0 i}{\frac{E-E_0}{\hbar} + \frac{i\gamma}{2}} \tag{11}$$

and the square of the amplitude gives the relative probability as

$$|A_E|^2 = \frac{A_0^2 \hbar^2}{(E - E_0)^2 + \left(\frac{\hbar\gamma}{2}\right)^2} \tag{12}$$

As $E = 2\pi\hbar f$ and by setting $f' = f - f_0$, we can write

$$\int_{-\infty}^{\infty} \frac{A_0^2 \hbar^2}{(E - E_0)^2 + \left(\frac{\hbar\gamma}{2}\right)^2} dE = \int_{-\infty}^{\infty} \frac{2\pi A_0^2 \hbar^3}{4\pi^2 (f')^2 + \left(\frac{\gamma}{4\pi}\right)^2} df' = \frac{A_0^2 \hbar^3}{2a} \tag{13}$$

In the previous integral, we used $\int_{-\infty}^{\infty} \frac{df'}{f'^2 + a^2} = \frac{\pi}{a}$ where $a = \frac{\gamma}{4\pi}$. To normalize the distribution in f, we find that $A_0^2 = \frac{2a}{\hbar^3}$ and the Lorentzian distribution for Natural line broadening f_L can be expressed as

$$f_{Lor,N} = \frac{a}{\pi} \frac{1}{\left(f - f_0\right)^2 + a^2} \tag{14}$$

where f_0 is the center frequency of the transition line.

1.5.2 Collisional Broadening

Electrons in the LIP are accelerated by the electric field of the plasma, continually acquiring energy until a collision occurs. Consider that the electrons collide with the heavy atoms and ions present in the plasma. Assume that the atoms and ions do not move as a result of the electron collisions. During an electron-atom collision, electrons within the atomic cloud absorb momentum from the free particle and excite to higher energy states. Over time, the electrons transition to lower excited states and emit a photon.

Let us define the probability that an electron will collide with a massive particle (atom or ion) [21]. The time between an electron colliding with a massive particle is τ, which is referred to as the relaxation time. The probability that an electron will collide with a massive particle in time Δt is $\Delta t/\tau$. The probability of an electron not colliding with a massive particle in time Δt is therefore $P(\Delta t)$ = 1 - $\Delta t/\tau$. Let us say that the probability of the electron not colliding with a massive particle after some time t is $P(t)$. The probability $P(t+\Delta t)$ that the electron does not collide with a massive particle after time $t + \Delta t$ can be expressed using the rule of independent probability.

$$P(t + \Delta t) = P(t)\Big(1 - \frac{\Delta t}{\tau}\Big) \tag{15}$$

Rearranging the terms and considering the limit as $\Delta t \to 0$, the previous expression can be written as

$$\frac{dP}{dt} + \frac{P}{\tau} = 0 \tag{16}$$

The solution to this first order linear differential equation is $P(t) = P_0 e^{-t/\tau}$. The distribution will be Lorentzian because the probability is decaying exponentially as in the case of natural broadening. The result for the collisional broadening can be obtained from the Lorentzian derived in the previous section and is

$$f_{Lor,C} = \frac{b}{\pi}\frac{1}{(f - f_0)^2 + b^2} \tag{17}$$

where $b = \frac{1}{4\pi\tau}$. The Lorentzian distribution is normalized for the integral of f_L for all time equal to 1. The only difference in the Lorentzian distributions between natural line broadening and collisional line broadening are the factors a and b. The natural and collisional line broadening half-widths a and b are typically 10^5 s^{-1} and 10^{13} s^{-1} for

Fe, respectively [22]. The spectrometer used in this thesis has a frequency resolution $\Delta f \sim 5 \times 10^{10}$ s^{-1}, so only collisional broadening effects were visible. For the purposes of this report, the visible Lorentzian broadening half-width will be defined as f_L.

1.5.3 Doppler Broadening

A population of emitting atoms that move with some velocity distribution relative to a detector will induce some broadening. A detector will record different frequencies of light f from two emitters moving with different line-of-sight velocities with respect to the detector. The Doppler frequency f for an atom (or ion) emitting light and approaching the detector with a velocity v is given by

$$f = \sqrt{\frac{1+\beta}{1-\beta}} f_0 \ , \quad \beta = \frac{v}{c} \tag{18}$$

where v is the velocity of the emitter and c is the speed of light and f_0 is the rest transition frequency of the emitter [23]. As the speeds v of the atoms or ions are much smaller than the speed of light, then the expression f can be expanded as a Taylor's series to the first order.

$$f \sim (1+\beta) f_0 \tag{19}$$

Therefore in 1-D,

$$v_x = c \frac{f - f_0}{f_0} \tag{20}$$

The population of emitters at a temperature T is given by the normalized 1-D Maxwell-Boltzmann distribution,

$$f_M = \left(\frac{m}{2\pi k_B T}\right)^{\frac{1}{2}} e^{-mv_x^2/2k_B T} \tag{21}$$

where the distribution is normalized to

$$\int_{-\infty}^{\infty} \left(\frac{m}{2\pi k_B T}\right)^{\frac{1}{2}} e^{-mv_x^2/2k_B T} dv_x = 1 \tag{22}$$

By replacing $dv_x = \frac{c}{f_0} df$ into Equation 22, we find that

$$\int_{-\infty}^{\infty} \left(\frac{1}{\sqrt{\pi} f_D}\right) e^{-(f-f_0)^2/f_D^2} df = 1 \tag{23}$$

The Doppler broadening distribution is then given by

$$f_{Dop} = \frac{1}{\sqrt{\pi} f_D} e^{-(\Delta f)^2/f_D^2}, \qquad f_D = \sqrt{\frac{2k_B T}{mc^2}} f_0 \tag{24}$$

where T represents the kinetic temperature of the plasma, m is the mass of the radiator, and Δf is the frequency shift from the rest frame transition frequency, f_0, caused by the velocity of the particle.

1.5.4 The Voigt Profile

Broadening effects which occur in a hot plasma produce two distinct line profile shapes, the Gaussian profile and the Lorentzian profile, depending on the environmental conditions present during photon emission. In practice, the normalized Gaussian and Lorentzian profiles convolve into the Voigt profile that is commonly seen in spectra [24].

$$f_{Voigt}(f) = f_{Lor}(f) \otimes f_{Dop}(f) \tag{25}$$

$$f_{Voigt}(f) = \frac{f_L}{\pi}\frac{1}{(f-f_0)^2+f_L^2} \otimes \frac{1}{\sqrt{\pi}f_D} exp\Big[-\Big(\frac{f-f_0}{f_D}\Big)^2\Big] \tag{26}$$

In cases where Gaussian FWHM is smaller than the Lorentzian FWHM, then the Voigt profile approaches a Lorentz profile in shape and amplitude. In such cases, then a Lorentz profile is sufficient for modeling the spectroscopic lines. However, in cases where the Gaussian FWHM is larger than the Lorentz FWHM, then the Voigt profile does not resemble either the Gaussian or Lorentzian line profiles. Within hot plasma, Stark broadening is mostly due to electron-ion impact under a strong electric field and the spectroscopic lines can usually be fitted to a Lorentzian profile.

1.6 Quantitative Analytic Procedures

Two primary methods of quantitative analysis exist for LIBS being calibrated and calibration-free LIBS.

1.6.1 Calibrated LIBS

Calibrated LIBS requires reference samples with known elemental concentrations to compare with the measured data of an unknown sample [12]. Calibration curves are produced for all emission lines of interest by plotting the line intensity against the concentration. The calibration curve will either be linear or quadratic depending on the laser-induced plasma conditions. The elemental concentration for each unknown sample is then determined by placing its line intensity on the calibration line. Including more reference samples on a calibration curve leads to more accurate results. It is difficult to produce calibration curves to exactly compare an unknown sample because of the matrix effect, where the contents of the sample can influence the signal of emission lines within the plasma. It is necessary to have many calibration curves of

various chemical compositions to best match the emission profile of a given sample. The study of calibrated LIBS tends to be easier with inorganic materials with simple matrix structures. Calibrated LIBS is especially useful for determining quality control in a manufacturing plant where the matrix structure is expected and consistent, and the spectra can be quickly compared to a reference chart.

1.6.2 Calibration-Free LIBS

Calibration-Free (CF) LIBS is the more complicated but more robust of the two methods of quantitative analysis for LIBS and avoids the matrix effect outlined below. CF-LIBS is used to analyze samples with complicated or unknown matrix structures, such as soil. Some initial assumptions of the plasma are required for CF-LIBS: the plasma production must be stoichiometric (a common assumption for plasma spectroscopy), the plasma must be in LTE and the plasma must be optically thin in the measuring regime. Plasma generated by laser irradiation is usually optically thin and transparent to the laser beam because the primary ionization process is through electron-atom impact. A laser beam could not help sustain plasma if the plasma were optically thick. Experimental results whose excited states satisfy the Boltzmann distribution generally indicates that the plasma is in LTE or pLTE. pLTE designates a plasma which shows characteristics of LTE that either is not in full LTE or is not possible to show full LTE.

The line emission intensity I_λ^{ki} produced by the transition between two states, E_k and E_i, of a species s is represented by the Saha-Boltzmann relationship as

$$I_\lambda^{ki} = FC_sA_{ki}\frac{g_k e^{-(E_k/K_BT)}}{U_s(T)} \tag{27}$$

where λ is the wavelength of the transition line, F is a parameter which accounts for the optical efficiency of the collecting system, C_s is the concentration of the emitting

species, A_{ki} is the transition probability from state k to state i, g_k is the k level degeneracy, T is the plasma temperature and $U_s(T)$ is the partition function for the species s at temperature T [25]. I_λ^{ki} is measured in counts/s. Equation 27 indicates that the population of electron states follows a Maxwellian distribution in LTE, the populations decrease exponentially with higher energy levels. Equation 27 can be rearranged into a linear equation.

$$y = ln\Big(\frac{I_\lambda^{ki}}{g_k A_{ki}}\Big) \tag{28}$$

$$x = E_k \tag{29}$$

$$m = -\frac{1}{K_B T} \tag{30}$$

$$b = ln\Big(\frac{FC_s}{U_s(T)}\Big) \tag{31}$$

$$ln\Big(\frac{I_\lambda^{ki}}{g_k A_{ki}}\Big) = \Big(-\frac{1}{K_B T}\Big)E_k + ln\Big(\frac{FC_s}{U_s(T)}\Big) \tag{32}$$

Equation 32 is used to generate a Boltzmann plot. The values I_λ^{ki} and E_k can be determined from a spectrogram and g_k and A_{ki} can be found online to plot the Boltzmann distribution. The excited temperature of the species are then found by measuring the slope, m, and solving Equation 30 for T. If the plot does not produce a linear relationship then one cannot assume the plasma is in LTE or pLTE because the population of electrons do not follow a Maxwellian distribution. The concentration of a species C_s (note, not quite the concentration of the element, just a species of the element) can be found by solving for the y-intercept, b, of the Boltzmann plot and the optical efficiency, F, of the spectrometer. To find F, note that the concentration across all species in the sample must sum to 1.

$$\sum_s C_s = \frac{1}{F} \sum_s U_s(T) e^b = 1 \tag{33}$$

The total concentration of a given element can be found by summing the partition functions across all species of a given element.

2 Experimental Setup

2.1 Experimental Setup

A Flare NX 1030-1.0.2 laser provided by Coherent induced a plasma on the surface of five stainless steel (SS304, SS309, SS316, SS330, & SS410) and four carbon steel (CSA2, CSAR500, CS4140 & High Carbon (CSHiC)) samples provided by McMaster-Carr. The Flare NX laser used in this thesis was linearly polarized and emitted in the infrared regime. An infrared laser was chosen for this experiment because the atmosphere is optically thin at 1 μm wavelengths. Particlarly, steel has a higher extinction coefficient in the near infrared than for visible wavelengths. The extinction coefficient k (the imaginary part of the refractive index) for iron is 3.91 at 1030 nm and 3.06 for a ruby laser at 632.8 nm [26]. A higher spectral intensity is required to ablate material using a red laser than an infrared laser due to the extinction coefficient. The Flare NX emitted laser pulses with a duration of about t = 1.5 ns at $\lambda = 1030 \pm 1$ nm and the energy per pulse was E = 527 μJ. Three lenses with focal lengths f_1 = 35 mm, f_2 = 400 mm, and f_3 = 100 mm focused the beam to a spot radius w_3 = 40 μm located 100 mm beyond f_3 as shown in Figure 2 (a). The first lens, L_1, was located a distance d_1 = 258 mm from the radiation source. L_1 and L_2 were positioned to expand the laser beam radius by a factor of about 11 and collimate the laser beam after it was transmitted through L_2. The second lens, L_2, located a distance d_2 = 432 mm beyond L_1, had a large focal length and radius of curvature and functioned to collimate the beam. The beam exited L_2 at a near normal angle and travelled a short distance d_3 = 98 mm to L_3. An infrared card was used at various points beyond lens L_2 to check that the beam was well collimated. Laser beam collimation was necessary to maximize the surface area of light on the third lens to reduce geometrical aberrations at the focal

point. The third lens, L_3, focused the beam at the target located a distance d_4 = 100 mm beyond the lens to a spot radius of ω_3 = 40 μm. Figure 2 shows an overhead view of the lens setup.

The steel samples were held in a metal casing and placed on three linear motorized translation stages moving in perpendicular directions (x, y and z). Each motorized stage travelled up to 25 mm and the set of three stages formed an orthogonal basis. The Z-translation stage, which moved along the beam axis, was placed about 10 mm behind the focal point of the laser to allow for measurements on both sides of the beam waist. The X- and Y-translation stages allow for radial movement across the beam axis so a fresh spot on the sample could be lased for each experimental run. The steel rusted after firing the laser at a given point on the sample and the same spot could not be analyzed multiple times, necessitating the use of the X- and Y-translation stages to move to another position on the sample as shown in Figure 2 (a).

The spectroscopic data was recorded using an iHR-320 spectrometer supplied by Horiba Canada. The iHR-320 provided a 0.06 nm resolution with a spectral range of 150-1500 nm. Light from the surface of the sample was captured by a telescope and fed through an optical fibre to the spectrometer pinhole. The telescope had a 38 mm focal length lens and was placed at roughly a 30° angle from the beam path and 92 mm from the tip of the optical fiber. The 38 mm focal length lens was chosen to expand the image of the plasma and maximize signal strength at the head of the optical fiber. Using Equation 34, the lens equation, we positioned the image of the plasma at the head of the fibre connected to the spectrometer, as shown in Figure 3.

$$\frac{1}{f} = \frac{1}{d_o} + \frac{1}{d_i} \tag{34}$$

The plasma produced on the sample is imaged at d_i = 92 mm for d_o = 65 mm at the

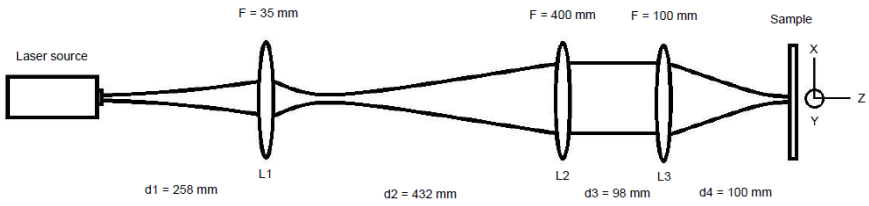

(a)

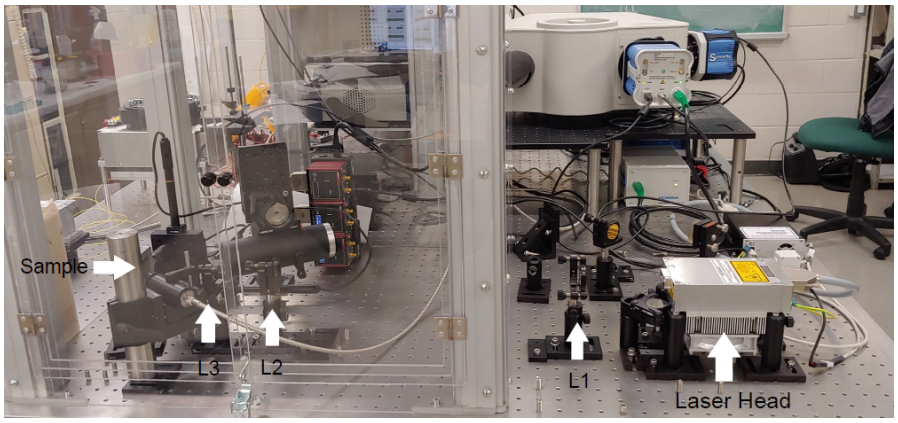

(b)

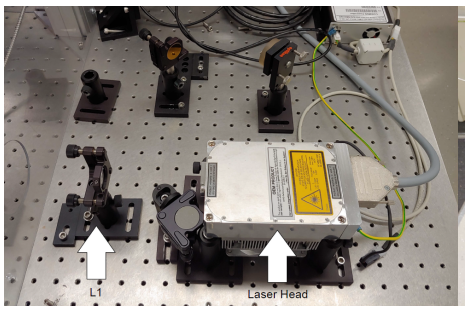

(c)

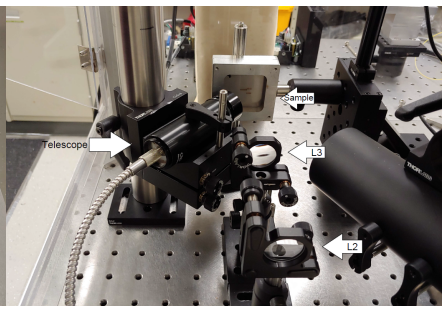

(d)

Figure 2: (a): An overhead schematic of the laser beam propagation from the laser head (left) to the steel target (right) through lenses L_1, L_2 and L_3.
(b): The experimental setup with the laser head on the right and the steel sample on the left. (c): A closer look at the laser head and the first lens, L_1. (d): A closer look at the sample after irradiation from the laser. Rusted marks are visible on the surface of the steel. L_2 is shown at the bottom of the image with L_3 directly above, and the telescope used for capturing light is shown on the left.

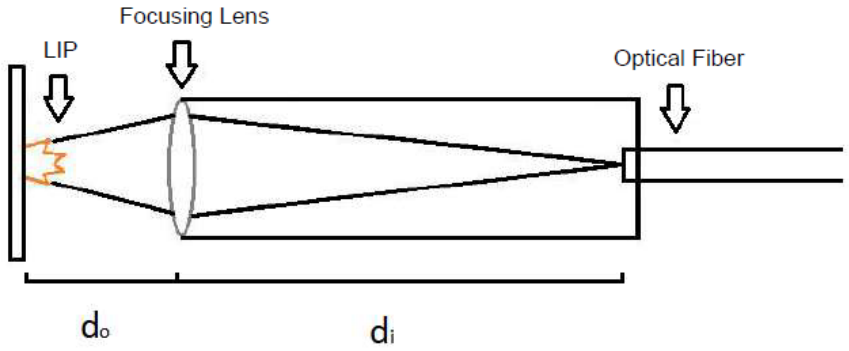

Figure 3: Light from the laser Induced Plasma (LIP) at the surface of the steel sample is focused to an image at the entrance of the optical fibre connected to the Horiba spectrometer.

head of the fiber. Placing the telescope at $d_o = 65$ mm maximized the intensity readings on the Horiba spectrometer.

Table 1: A list of all steel samples analyzed in this investigation. The corresponding chromium and iron concentrations given by the manufacturer are listed.

Sample	Cr Concentration (%)	Fe Concentration (%)
SS304 (8983k125)	17.5 - 24	53.5 - 74.5
SS309 (9021N1)	24 - 26	47.8 - 57
SS316 (88885k74)	16 - 18.5	58.3 - 73.6
SS330 (3656N1)	18 - 20	38.4 - 43.9
SS410 (SDK322861)	11.9	87
CSA2 (89885K16)	4.75 - 13	86 - 95
CSAR 500 (4170N111)	0.75	97
CSHiC (2953N116)	0	97
CS4140 (4473T31)	0.75 - 1.2	97

Steel samples, which are listed in Table 1, were held in a sample holder to be irradiated by the laser for this investigation. The steel samples were cut into 2" × 2" squares and were obtained from McMaster Carr. Table 1 also shows the chromium (Cr) and iron (Fe) concentrations given by the manufacturer.

2.2 ABCD Matrix to define the laser beam

In order to produce a sufficient power density to ionize the surface of steel, the laser needed to be focused to a small beam spot. The ray transfer of 2×2 (ABCD) matrix technique was used to model the path of the laser and to determine an environment that sufficiently focused the beam. The ABCD matrix technique treats sections of the laser setup in Figure 2 (a) independently. Seven sections existed in this experiment, consisting of four free space and three thin lens sections. Free space is interpreted as a simple refraction through a medium (air) as the light propagates. The spherical biconvex lenses used in this experiment are approximated to be thin lenses. The (ABCD) matrix is valid for paraxial approximation (for angles less than 15 degrees), which is the case for focused rays propagating and focused in the set-up shown in Figure 2 (a).

The ABCD matrix element of a laser beam travelling through a distance d of transparent medium n is described by the transfer matrix

$$\begin{pmatrix} 1 & \frac{d}{n} \\ 0 & 1 \end{pmatrix} \tag{35}$$

and the ABCD matrix for a thin lens with a focal length of f is given by

$$\begin{pmatrix} 1 & 0 \\ -\frac{1}{f} & 1 \end{pmatrix} \tag{36}$$

To determine how a laser beam will behave in a system, we multiply the corresponding sequence of ABCD transformation matrices to determine the total transfer matrix, M. For this thesis, a system of three lenses and four propagation zones exist

between the laser and the target for a product of seven matrices to obtain M as shown in Equations 37 and 38. Therefore, the beam satisfies the following transformation matrix sequence

$$\begin{pmatrix} x_2 \\ \bar{x}_2 \end{pmatrix} = M \times \begin{pmatrix} x_1 \\ \bar{x}_1 \end{pmatrix} \tag{37}$$

$$M = \begin{pmatrix} 1 & d_4 \\ 0 & 1 \end{pmatrix} \begin{pmatrix} 1 & 0 \\ -\frac{1}{f_3} & 1 \end{pmatrix} \begin{pmatrix} 1 & d_3 \\ 0 & 1 \end{pmatrix} \begin{pmatrix} 1 & 0 \\ -\frac{1}{f_2} & 1 \end{pmatrix} \begin{pmatrix} 1 & d_2 \\ 0 & 1 \end{pmatrix} \begin{pmatrix} 1 & 0 \\ -\frac{1}{f_1} & 1 \end{pmatrix} \begin{pmatrix} 1 & d_1 \\ 0 & 1 \end{pmatrix} \tag{38}$$

which can be shown to reduce to

$$\begin{pmatrix} x_2 \\ \bar{x}_2 \end{pmatrix} = \begin{pmatrix} A_7 & B_7 \\ C_7 & D_7 \end{pmatrix} \times \begin{pmatrix} x_1 \\ \bar{x}_1 \end{pmatrix} \tag{39}$$

where

$$A_7 = \beta d_4 + \left(1 - \frac{d_4}{f_3}\right)\left(\beta d_3 + 1 - \frac{d_2}{f_1}\right) \tag{40}$$

$$B_7 = \alpha d_4 + \left(1 - \frac{d_4}{f_3}\right)\left(\alpha d_3 + d_1 + d_2 - \frac{d_1 d_2}{f_1}\right) \tag{41}$$

$$C_7 = \beta - \frac{1}{f_3}\left(\beta d_3 + 1 - \frac{d_2}{f_1}\right) \tag{42}$$

$$D_7 = \alpha - \frac{1}{f_3}\left(\alpha d_3 + d_1 + d_2 - \frac{d_1 d_2}{f_1}\right) \tag{43}$$

$$\alpha = 1 - \frac{d_1}{f_1} - \frac{d_1}{f_2} - \frac{d_2}{f_2} + \frac{d_1 d_2}{f_1 f_2} \tag{44}$$

$$\beta = \frac{d_2}{f_1 f_2} - \frac{1}{f_1} - \frac{1}{f_2} \tag{45}$$

The complex radius of the Gaussian beam is given by [23]

$$\frac{1}{\tilde{q}(z)} = \frac{1}{R(z)} - i\frac{\lambda}{\pi\omega^2(z)} \tag{46}$$

where R(z) and ω(z) are the radius of curvature and the beam radius at some point z along the path of propagation. The propagation formula for a beam passing through f_3 is given by

$$\tilde{q}_3 = \frac{A\tilde{q}_0 + B}{C\tilde{q}_0 + D} \tag{47}$$

where A, B, C and D are the elements from the ABCD matrix derived in Equations 40 to 43. $\tilde{q}_0$ is the complex radius of the beam within the laser head and $\tilde{q}_3$ is the complex radius of the beam at the the focal point beyond the lens L_3. The final beam waist ω_3 produced by the ray transfer matrix M is given by

$$\omega_3 = \omega_0\left(A_7^2 + \left(\frac{B_7}{\delta_L}\right)^2\right)^{0.5} + A_b\ , \quad \delta_L = \frac{\pi\omega_0^2}{M^2\lambda} \tag{48}$$

where the first term on the RHS in Equation 48 is the spot size predicted by the ABCD paraxial approximation. δ_L considers that the beam is not perfectly Gaussian. The M^2 term refers to the beam quality given by the manufacturer, $M^2 = 1.07$, and is not the beam transfer matrix. The second term on the RHS of Equation 48, A_b, is an approximation of aberrations produced by the spherical biconvex lenses used in this experiment. Aberrations form because a biconvex lens is not perfectly thin and this value is an estimate given by the manufacturer. Aberrations are calculated through

$$A_b = A \times \frac{f^3}{D^2} \tag{49}$$

where A is a constant given by the manufacturer, f is the focal length of the lens and D is the diameter of the lens filled by the laser beam. Calculating the aberrations in this case only gives an estimate based on the manufacturers value and will be determined from the beam profiling results in Section 2.3.

2.3 Beam Profiling

A knife-edge method was used to measure the beam spot size at various locations with respect to the focal point to confirm that the ABCD matrix technique is accurately describing the beam [27]. An S314C model thermopile was placed behind the knife blade to measure the laser beam intensity both in front of and behind the laser spot, ω_3. The thermopile was connected to a PM100/PM200 monitor. Thermopiles convert temperature from absorbed photons to an electrical current which is read as intensity. Thermopiles do not measure spatial resolution and it could therefore only determine total intensity of the beam when the beam was partially intercepted by the blade. The diameter of the laser beam was found by employing the knife-edge method by sliding the knife across the beam axis and recording the intensity readings from the thermopile. The knife is a razor blade connected to a post and is moved across the laser beam in a direction that is perpendicular to the beam propagation direction. The blade connected to the post is moved using the orthogonal motorized translation stages to measured accurate positions. At first, the intensity of the beam I_0 was measured without any interference from the knife. Then, the $1/e^2$ 90th and 10th percentile intensities of I_0 were measured, as shown in Figure 4. By moving the blade along the X-axis, the locations which reduced the beam intensity to 90% and 10% of I_0 were recorded.

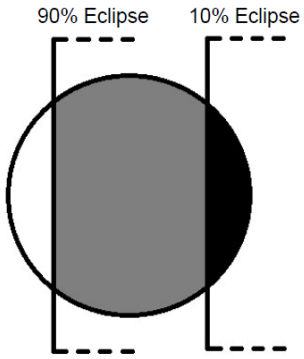

Figure 4: The knife blade, represented by the vertical and dashed lines, was used to block the Gaussian laser beam. The specified locations of three intensity measurements (0% eclipse, 10% eclipse, 90% eclipse) were recorded using a thermopile to determine the diameter of the beam as a function of distance.

The difference of the knife position which produced I_{90} and I_{10} was the diameter of the beam at position z. This process was iterated at various z positions to find how the beam propagates along z. All measurements are listed in Table 2.

Accounting for aberrations, the best fit beam spot size at the focal point is about 0.0011 cm in radius giving a spot area of 3.8×10^{-6} cm^2. It can be seen in Figure 5 that the paraxial approximation exceeds the experimental data for most points. A possibility for this is due to the beam quality supplied by the manufacturer. All commercially manufactured lasers have an asymmetric Gaussian beam. Manufacturers include information on the beam quality, M^2, to indicate the axial symmetry of the beam. For the laser used in this experiment, a beam quality of $M^2 = 1.07$ was supplied, indicating some asymmetry was present in the beam. Now, only one axis of the beam was measured with the knife-edge method. It is possible that the asymmetry of the beam gave a narrower result than the M^2 parameter would normally indicate. The supplied M^2 parameter was not measured per unit, so some discrepancies could exist across the sample of lasers produced. For example, an M^2 value of 1.02 produced a paraxial

Table 2: The laser beam diameter (mm) at all Z positions (mm) from the home location of the motor stage. A 10% uncertainty was applied to each diameter to account for aberrations.

Z Position (mm)	**Diameter (mm)**	**Z Position (mm)**	**Diameter (mm)**
0	0.488	14	0.276
1	0.449	15	0.339
2	0.374	16	0.381
3	0.337	17	0.437
4	0.271	18	0.496
5	0.223	19	0.564
6	0.165	20	0.612
7	0.122	21	0.651
11	0.127	23	0.768
12	0.175	25	0.891
13	0.222		

approximation narrower the experimental points. Regardless, the fit is quite good and gives an accurate estimate of the beam waist ω_3.

Aberrations and beam quality are not the only uncertainties to consider. As can be seen in Figure 5, close to ω_3, the measured beam diameter on the RHS of ω_3 deviates slightly from the predicted beam diameter. The measured beam diameter is narrower on the RHS than on the LHS of the focal point when compared to the ABCD paraxial approximation. This possible source of uncertainty comes from the angle that the knife edge is held relative to the beam axis. Small variations in the angle of the knife can over or underestimate the diameter of the beam, depending on the orientation of the knife. Figure 6 shows how tilting affects the beam diameter measurements. Tilting has been greatly exaggerated for the sake of clarity. For example, the goal of using the Knife-edge method was to measure the beam diameter at locations z_1, z_3, and z_5. Due to the natural beam divergence, a small positive change in the angle of the knife blade will give true locations of the knife blade at z_2, z_4, and z_6, as shown in Figure 6. Once the knife was in position, it was only moved by a motorized stage. Any tilting

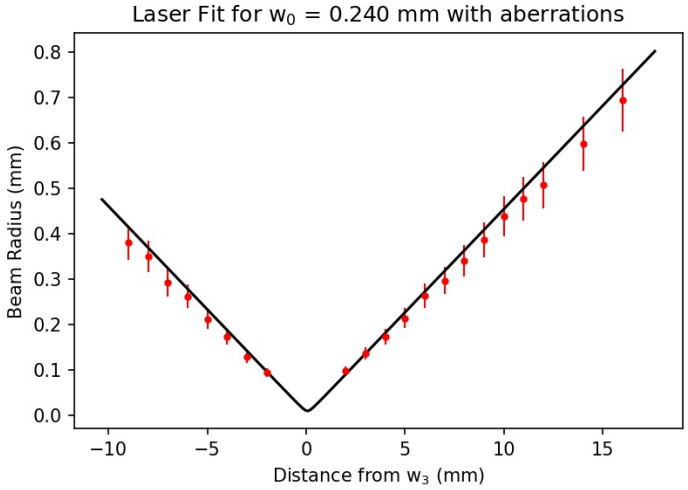

Figure 5: The theoretical beam profile across the focal point was calculated using Equation 48 and is shown with the black line. The measured beam radii listed in Table 2 are shown as red points with uncertainties shown by vertical lines. The beam waist has an approximately 0.011 mm radius.

present was held constant through the analysis. In the region between lines 1 and 2, the blade will measure a smaller beam radius by a distance of Δz_n for locations z_n until the Rayleigh zone. This is a systematic process and results in a negative uncertainty left of the beam waist in Figure 5. Within the Rayleigh zone of lines 3 and 4, the beam is quite straight and almost no systematic uncertainty would be measured. Plasma was produced on the knife blade within 3 mm of the beam waist ω_3, so measurements within the Rayleigh zone were not available in Table 2. Beyond the Rayleigh zone near lines 5 and 6, a beam radius with a positive Δz_n would be systematically measured due to the positive tilt on the knife edge. The uncertainty due to the knife angle is small for a narrow beam with a small radius of curvature but increases as the beam diameter increases. The uncertainty gets larger as the radius of curvature of the beam continues to grow. A negative angle on the knife edge would measure a systematically wider beam before ω_3 and a narrower beam beyond ω_3.

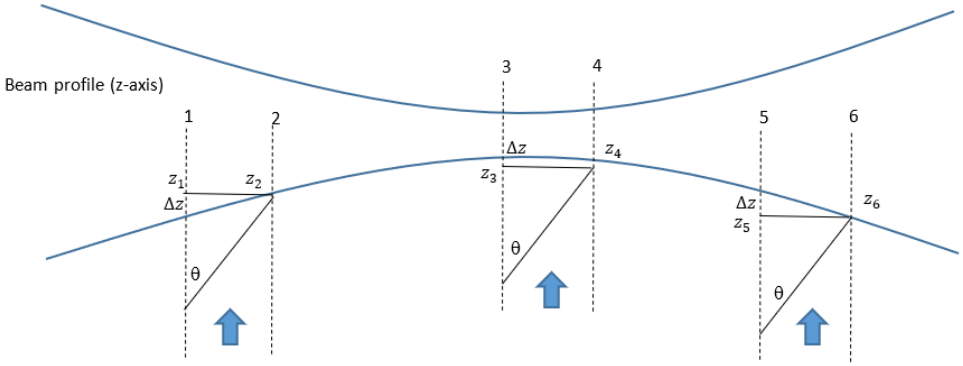

Figure 6: Tilting of the knife blade at locations z_1, z_3 and z_5 would result in beam radius measurements being recorded at locations z_2, z_4 and z_6, respectively. The systematic error would produce a negative statistical uncertainty to the left of the Rayleigh zone and a positive statistical uncertainty to the right of the Rayleigh zone.

2.4 Power of the Laser

The laser used in this investigation was pulsed at a repetition rate of 2000 Hz with an average power of 1.055 W and a pulse duration of 1.45 ns. A total of 527.5 μJ of energy was released in every pulse to achieve an average power of 1.055 W. One can divide the energy per pulse by the time duration of the pulse to find the mean peak power of the laser (the power while actively emitting), $P_M = 3.6 \times 10^5$ W. The beam waist ω_0 is 0.48 mm in diameter and is located inside the laser head. The peak power density can be calculated by dividing the peak power by the beam cross section at the focal point ω_3. The beam spot radius is 11 μm, then the peak power density is calculated as:

$$P_{Peak} = \frac{P_M}{\pi\omega_3^2} = 9.5 \times 10^{14} \frac{W}{m^2} \tag{50}$$

The power flow of the laser beam is represented by the Poynting vector, **S**, and is found through the electric field strength of the beam, **E**.

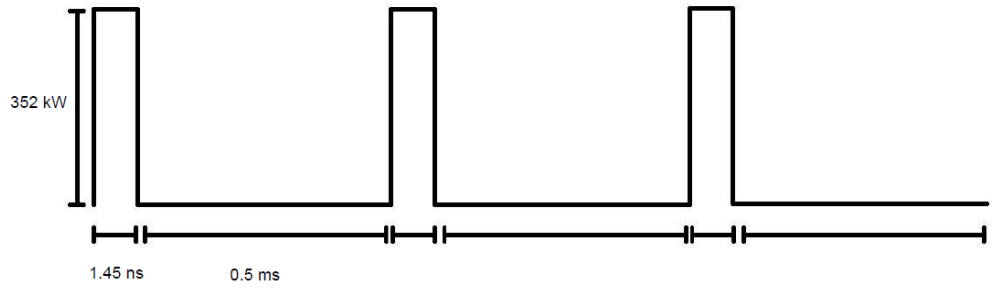

Figure 7: The laser pulses for 1.45 ns every 0.5 ms (2000 Hz) with a pulse height of 3.52×10^5 W. Each laser pulse contains 527.5 μJ of energy.

$$\mathbf{S} = \frac{c\epsilon_0}{2}|\mathbf{E}|^2 \tag{51}$$

While knowing the peak power density, $\mathbf{S} = 9.5 \times 10^{14}$ W m^{-2}, we can rearrange Equation 51 to solve for the peak electric field strength, $\mathbf{E} = 8.5 \times 10^8$ V m^{-1}. An electric field on the order of 7×10^7 V m^{-1} is required to ionize electrons from the surface of stainless steel and an electric field of 3×10^6 V m^{-1} is required to ionize electrons from the air [28, 29]. Plasma was visibly generated both on the surface of the steel and in the air while no sample was within the focal point of the laser. All values were converted and calculated in MKS notation.

When a steel sample was positioned at the focal point, atoms were ionized by the electric field. After atoms were ionized by the electric field as a result of collisions and heat transfer at the surface of the steel, the electrons could recombine and emit spectroscopic lines when transiting from an upper to lower level energy states. As energy states are not the same across different atoms, it was possible to identify the main and alloying elements of a given sample from the obtained spectroscopic line signature on the spectrograms.

2.5 Q-switched lasers

There are active and passive methods of creating a time delay for data acquisition using a Q-switch. Active methods of Q-switching are common and rely on modulating the laser transmission using a high frequency RF signal. A diagram of an active Q-switched laser is given in Figure 8. The light created in the crystal is passed through a linear polarizer after emission and then followed by a Pockels cell (PC). A PC is a linear polarizer that changes its axis of polarization when a voltage is applied. At maximum voltage, the polarization axis of the PC is perpendicular to the crystal polarizer and the laser transmission is zero. At zero applied voltage, the polarization axis of the PC aligns with the polarization axis of the emitted light and transmission is maximum. In an active Q-switched pulse laser, the pulse is modulated by a square wave RF signal to control the repetition rate and pulse duration of the laser pulse. The square RF signal is sent from an external modulator that also sends a manually controllable, delayed signal to begin data acquisition by the spectrometer.

Passive Q-switching relies on an absorber to naturally gate the laser emission. Similar to an active modulator, an absorber is placed in the path of the laser and blocks transmission while a condition is held. An emission above a certain threshold intensity pumps electrons in the absorber from ground states to excited energy states. Once the ground states are used up, the transmission increases rapidly in the absorber for a few nanoseconds and a pulse of light is emitted [30]. The excited electrons in the absorber quickly transition back to the ground states and lower the transmission rate of the absorber, emitting light in the process. Passively pulsed lasers act on this absorption-emission cycle to create an accurately pulsed laser. Passive Q-switches are smaller than active Q-switches and require no external modulation. The semiconductor saturable absorber material (SESAM) used for passive Q-switching can be tuned across a

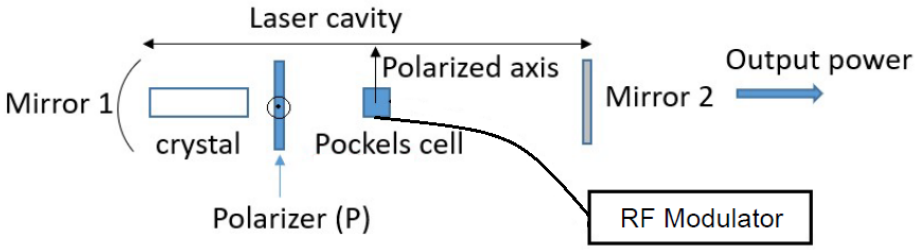

Figure 8: An example of how an active Q-switch is structured inside a laser cavity. At maximum voltage, the polarized axis of the Pockels cell is perpendicular to the linear polarizer as shown in the figure and transmission is zero. At zero voltage, the polarized axis flips to become perpendicular to the page and aligned with the linear polarizer, allowing maximum transmission of the laser.

short band of wavelength [31]. The laser used in this thesis is a passively Q-switched diode pumped solid state laser.

2.6 Laser Induced Plasma Spectroscopy

Laser induced breakdown spectroscopy (LIBS) and the laser induced plasma spectroscopy (LIPS) technique used in this investigation are distinct analytical methods whose differences will be outlined below. The laser induced plasma dynamics for LIBS and LIPS will also be described further in this section.

LIBS typically uses a higher energy laser pulse (~50 mJ), pulses at a low repetition rate (~10 Hz), and the pulse length in a LIBS experiment is usually 5-10 ns. These parameters are used to ensure a hot plasma is produced at the surface of the target and that the plasma de-excites completely before subsequent laser pulses, which usually takes about 10 μs [12]. LIBS experiments typically use an active laser Q-switch to delay any data acquisition by a spectrometer. The laser used in this LIPS report has a weaker laser pulse (~0.5 mJ) and pulses at a much higher repetition rate (~2000 Hz) than LIBS experiments. The laser pulsed every 50 μs for 1.5 ns, which allowed

enough time for the plasma to de-excite completely before the next pulse. The laser beam was focused to a spot radius of 40 μm and was beyond the threshold intensity to produce a plasma as shown in Section 2.4. The LIPS system in this report did not use a Q-switched mechanism to delay data acquisition.

The strong electric field at the focal point of the laser stripped electrons from the conduction band of the steel to begin plasma formation. The electrons accelerate to high velocities and temperature, heating the surface of the steel to melt and evapourate atoms from the crystalline structure. The electrons then cool over time through collisions with free ions, atoms and other electrons, distributing energy throughout the plasma. A sufficiently dense plasma typically reaches Local Thermal Equilibrium (LTE) after ~100 ns [12]. At this point, plasma expansion has ceased and one single temperature typically describes the electrons, the atoms and the ions within the plasma. In LIBS systems, time delayed spectroscopic data acquisition can measure the properties of the plasma at various times to ensure a uniform temperature exists. After laser emission has ceased, collisional excitation dominates and sustains the plasma. Spontaneous atomic de-excitation transfers energy out of the plasma to slowly cool the plasma. In LIBS, a Q-switched gating mechanism delays spectroscopic data acquisition until LTE has been reached to measure the dynamics of the plasma. Light produced from atomic de-excitation in LTE is mainly captured by the spectrometer, though some broadband thermal emission exists. Figure 9 shows how data acquisition is timed using a delay gate Q-switch in a typical LIBS experiment. In Figure 9, the laser emits a high energy pulse (50 mJ) with a duration of 10 ns at a repetition rate of 10 Hz. Data acquisition begins around 1 μs after laser emission after the plasma has entered LTE. In LIPS, no time delay is used and all light is captured by the spectrometer, including the broadband thermal noise from electrons during the plasma expansion

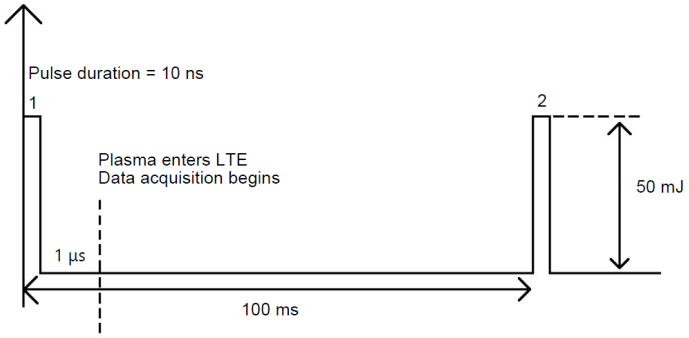

Figure 9: The typical dynamics of a LIBS experiment. The laser typically pulses for 10 ns with a 50 mJ pulse height. After about 1 μs, the plasma is in LTE and the delay gate modulator triggers data acquisition to begin. LIBS works with a small repetition rate to ensure the plasma cools before re-emission.

before LTE conditions exist. The delay produced from a Q-switch becomes unreliable in applications where turbulence and thermal blooming exist such as aiding long distance remote sensing projects. It is not easy to model the path of the laser beam and the location of the focal point may vary with turbulence, slowing a predicted plasma production. Therefore our investigations using LIPS should be useful when gathering at long distance using a laser at a high repetition rate

2.7 Spectroscopic Data Acquisition

The Horiba iHR-320 spectrometer used in this thesis is a classic Czerny-Turner spectrometer [32]. The spectrometer used a planar grating and two spherical mirrors to focus the light on the cooled CCD as shown in Figure 10 (a). L_{EC}, L_{CG}, L_{GF}, and L_{FD} are the distances from the entrance pinhole to the collimating mirror, the collimating mittor to the grating, the grating to the focusing mirror and the focusing mirror to the detector, respectively. α_C is the incident angle of the incoming light with respect to the collimating mirror and α_F is the incident angle of light from the grating to the focusing

mirror. R_C and R_F are the radii of curvature for the collimating and focusing mirrors. i is the incidence angle for the diffraction grating and θ is the angle of diffraction. β is the angle of reflection from the focusing mirror. The decenter D relates to the spectral resolution of the spectrometer. A longer distance L_{GF} can allow the light to spread further by increasing the value of D. In Figure 10 (b), the length of the spectral image L that is produced is related to the decenter by

$$L = D_{B_{max}} - D_{B_{min}} \tag{52}$$

The Horiba iHR320 spectrometer had a plane grating of 1200 lines per mm and was used to disperse the light into a CCD camera cooled to -60 °C. The light captured by the telescope discussed in Section 2.1 was delivered to the spectrometer by a 600 μm optical fiber. Inside the spectrometer, the light was reflected off a collimating mirror and directed toward a diffraction grating to disperse the light as a function of wavelength. The light was then focused by a mirror to create an image on the surface of the cooled CCD camera. The light travelled a distance of about 320 mm within the spectrometer before reaching the CCD camera to produce a wavelength resolution of about 0.05 nm. The spectrometer was calibrated using a blue multi-line argon laser with peaks at λ_1 = 457.9 nm, λ_2 = 476.5 nm, λ_3 = 488 nm, λ_4 = 501.7 nm and λ_5 = 514.5 nm. The light diffracted off the plane grating according to the Bragg relation,

$$n\lambda = 2dsin(\theta) \tag{53}$$

where n is the diffraction order, λ is the wavelength of the incident light, d is the grating constant and θ is the angle of diffraction. The grating constant d refers to the spacing between lines on the grating and was d = 1 mm/1200 $\sim$ 833 nm in this experiment.

Higher orders of refraction were not captured by the cooled CCD camera, they were refracted at a higher angle θ away from the detector. The CCD only captured light within a 60 nm band to avoid the higher diffraction orders. The vertex and wavelength segments for the off-axis parabolic mirror (OAP) are shown in Figure 10.

The system was controlled by a script written in LabView 2017. User input dictated the duration of lasing and the repetition rate that the laser operates at, which were 5 s and 2000 Hz, respectively. The spectrometer was set to integrate the captured light over a 0.025 second integration block and to repeat for 30 integration blocks, resulting in a 3-dimensional plot showing how the spectrum evolved over time.

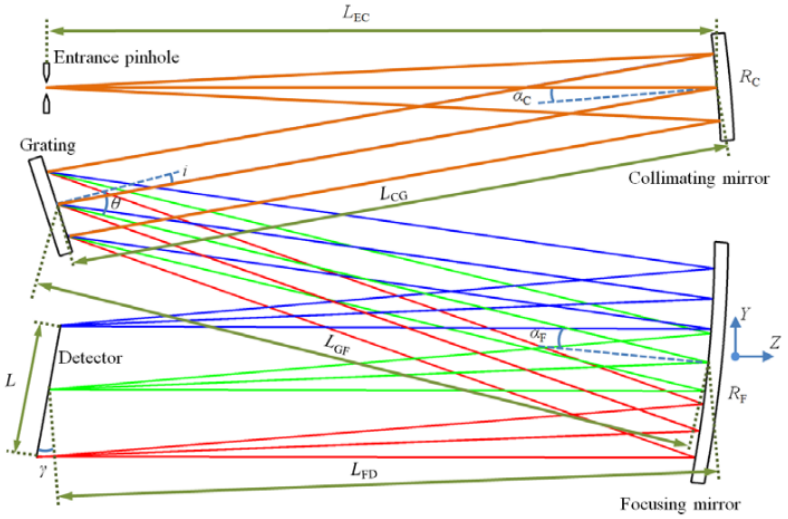

(a)

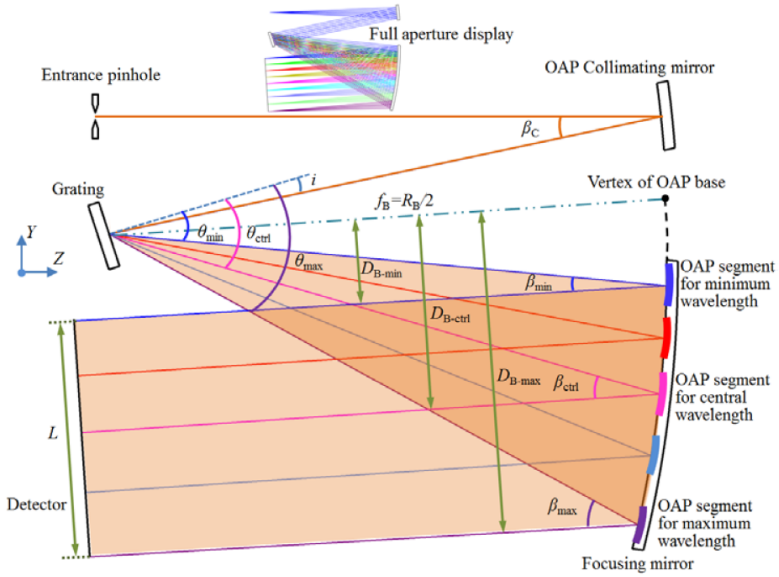

(b)

Figure 10: (a) The structure of a Czerny-Turner spectrometer. (b) The structure of a Czerny-Turner spectrometer highlighting how the decenter D relates to spectral resolution. Note that the vertex and the wavelength segments for the off-axis parabolic mirror (OAP) are shown. Reprinted from (32).

3 Spectroscopic Results

3.1 Analysis

For the purposes of this section, a 'data set' will refer to the set of spectrograms recorded during an individual 'run' of the experimental setup. Within a run, the laser ablated the surface of a steel sample for 5 seconds and the spectrometer was turned on manually just before ablation began. The spectrometer recorded 30 spectrograms with an integration time of 0.025 seconds per spectra to produce a data set. If the spectrometer was accidentally turned on after ablation began, then the data set was discarded, the steel was moved so that a fresh spot would be lased and the run was restarted. Typically, a program could automatically start the spectrometer with a command to start the laser, but it was easier to manually start the spectrometer before the laser. This was more convenient and avoided any loss of information due to delays between the laser and start of the spectrometer data acquisition. The spectrometer's wavelength range was manually set for each run and spanned 60 nm in wavelength as shown in Figures 11 and 12. The data sets were recorded in the form of histograms, measuring the number of photon interactions (counts) per pixel on a CCD cooled to -60 °C. The grating within the spectrometer diffracted light as a function of wavelength which allowed the pixels to represent wavelength on the x-axis of the spectrograms. The spectroscopic signal quickly increased during the first three to four spectrograms. The signal did not immediately record at a maximum value. It took time for the plasma to grow due to the heat capacity of steel. The energy required to vapourize the target of steel within the focal point of the laser is given by

$$\Delta E = mc\Delta T + mH \tag{54}$$

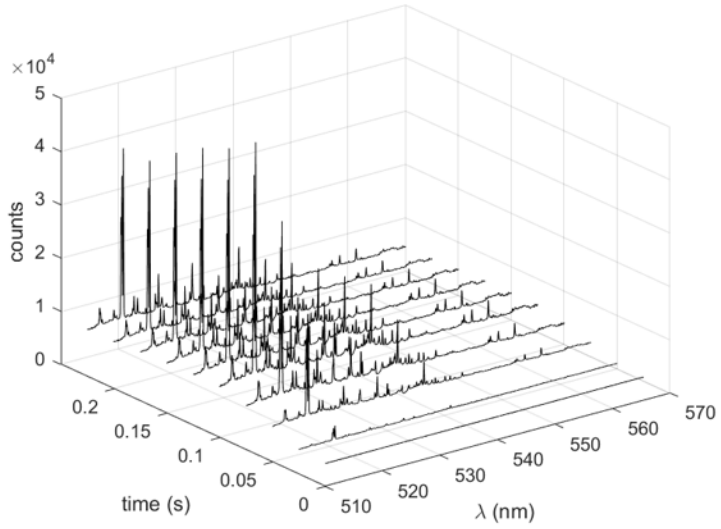

Figure 11: A series of ten spectrograms were produced from a sample of SS 304 with an integration time of 0.025 s. The spectroscopic signal increases rapidly to a peak during the first five spectrograms before slowly declining over time.

where ΔE is the vapourization energy, m is the mass of the system heated, c is the heat capacity of the system, ΔT is the change in temperature required to vapourize, and H is the specific heat required to vapourize the system. The first term on the RHS of Equation 54 is the amount of energy required to heat a system to the vapourization temperature. The second term on the RHS of Equation 54 is the added amount of energy required to vapourize a system at the target temperature, such as the boiling point.

The heat of vapourization (H) of iron is 6.34×10^6 J kg^{-1}, the specific heat (c) of iron is about 450 J kg^{-1} K^{-1} and the density (ρ) of iron is 7.87×10^3 kg m^{-3} [33, 34]. Using a focal radius (ω_3) of 11 μm as derived in Section 2.3, the volume of the target can be approximated to 3.8×10^{-16} m^3 by assuming a depth of 1 μm was ablated per pulse. By multiplying the volume by the density of iron, a mass (m) of 2.99×10^{-12} kg

can be used to find ΔE in Equation 54. The boiling point (T_B) of iron at atmospheric pressure is about 3135 K, so ΔT was about 2840 K when the steel was ablated at room temperature. Using Equation 54, an energy of $\Delta E \approx 2.28 \times 10^{-5}$ J or 22.8 μJ was required to vapourize a cylinder of steel with a volume of 3.8×10^{-16} m^3.

The values of H, c and ρ listed above are those of iron. The steel samples used in this thesis had varying levels of iron and chromium concentrations and would therefore all have slightly different boiling points, specific heats and heats of vapourization. The calculation was used as an example to show the scale of energy required to vapourize an iron-based material within the focal point of the laser. The energy required for vapourization (ΔE = 22.8 μJ) is much smaller than the energy per pulse (500 μJ). The laser vapourized the system very easily to produce a plasma.

The system clearly did not take a long time to vapourize the assumed mass. However, vapourization accelerated across 3-4 spectrograms in Figure 11 as the volume of the system that was vapourized increased toward an equilibrium. It took time for the system to reach a maximum amplitude, where the flow of material into the plasma reached an equilibrium with matter outflow from the plasma. The laser pulsed 50 times within the integration block of each recorded spectrogram

$$N_{Pulses} = f \times t \tag{55}$$

where f is the frequency the laser pulsed at (2000 Hz), t is the integration time of a spectrogram (0.025 s) and N_{pulses} is the number of pulses per spectrogram (50). As matter was ablated per pulse, an optically thin plasma was formed from the vapourized Fe and Cr atoms. Electrons within the plasma absorbed light from the laser to accelerate plasma growth. The plasma then cooled between pulses, depositing some of the material on the surface of the target. Some material vapourized by a pulse was

not available for each subsequent pulse to ionize and needed to be re-vapourized by the subsequent pulse, slowing the growth of the plasma.

After a maximum signal was reached, the spectroscopic signal slowly decreased over time as the laser ablated a deeper hole in the steel. The size of the hole ablated by the laser ($\sim 50\,\mu$m) was on the order of the wavelength of the laser (1.03 μm). This will be discussed further in Section 4.2. Deep in the hole, diffraction began to dampen the intensity of the laser and slowed the vapourization process. Less free particles were available to sustain the plasma. Additionally, rust began to deposit on the surface of the steel over time. Free Fe I ions combined with free O I ions in the atmosphere to form rust, some of which deposited on the steel surface. Rust is more difficult to ablate than steel due to its molecular structure, as discussed in Section 1.3.2, and further limited the production of free Fe and Cr atoms required to sustain the plasma. Over time, the plasma weakened and produced a smaller spectroscopic signal.

Example spectrograms for SS304 and CSAR500 are shown in Figure 12 (a) and (b), respectively. These two steels were chosen to be contrasted because SS304 has a high concentration of Cr (~20%) while CSAR500 has a low concentration of Cr (~0.75%). It is clear to see the different amplitudes produced by the Cr I emission lines between the two samples. The structure of the broadband noise is difficult to see in Figure 12 because the spectra are located near the peak of the thermal curve and span only 60 nm of wavelength. The thermal emission curve amplitude is approximately 6000 counts and the spectroscopic lines are visible above the curve in Figure 12. It is possible to determine the elemental concentration of non-trace elements with the presence of thermal noise.

The intensity (counts) of the Cr I 520.84 nm and the Fe I 526.91 nm lines were measured for each sample to produce the chemical concentration graphs shown in Fig-

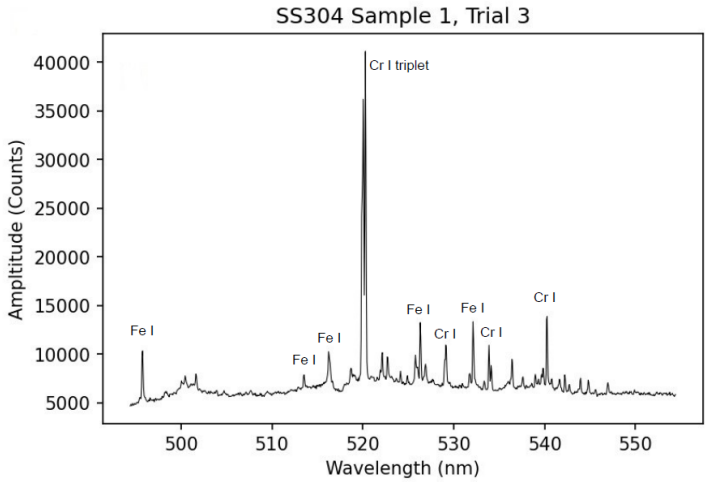

(a) The Spectrum of SS304 between 494 nm - 554 nm.

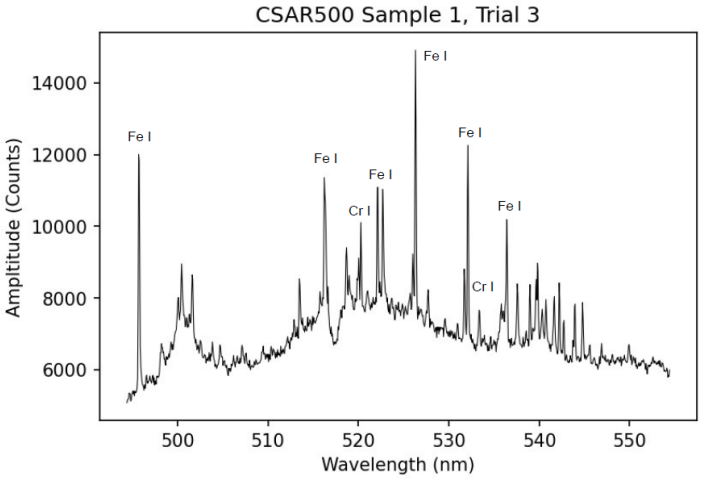

(b) The Spectrum of CSAR500 between 494 nm - 554 nm.

Figure 12: Example spectra of (a) SS304 and (b) CSAR500. The spectrometer grating is parked at 525 nm. Note that the peak emissions are superimposed on to a thermal curve from Planck's radiation law, which is more obvious for CSAR500.

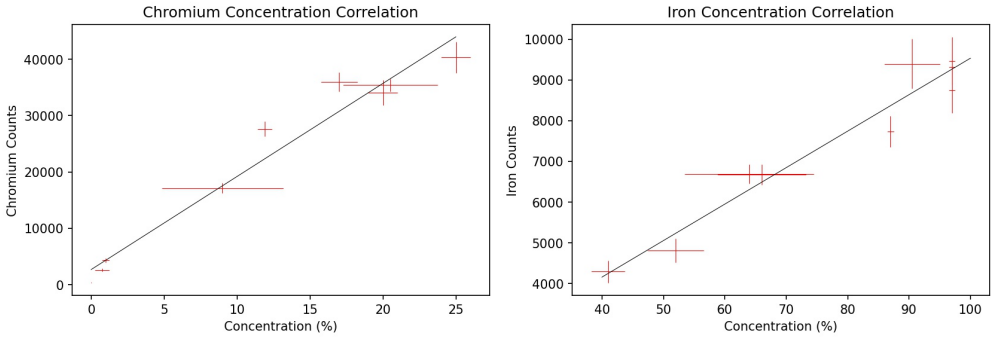

(a) (b)

Figure 13: Graphs of mean spectroscopic line counts from all 9 types of steel plotted against the manufacturer's claimed concentrations for (a) Cr 520.84 nm and (b) Fe 526.91 nm.

ure 13, which compare the average counts for each sample from the spectra with the manufacturers reported elemental concentration for the given species. The Cr I 520.84 nm and Fe 526.91 nm lines were selected for analysis due to their high relative intensity. A linear trend appears in the data and a line of best fit can be applied to determine how the counts are related to the concentration. There are two goals in producing this graph. First, if at least two reference samples are available with known elemental concentrations then the concentration of each unknown sample can be estimated. This idea is similar to the calibrated LIBS method discussed in Section 1.6.1 but it is presently only applicable to inorganic materials with simple chemical matrices. Second, a limit of detection (LOD) can be determined for each element present in the sample. The LOD represents the minimum concentration of a given element that can be resolved as a line in the spectrogram. The LOD will be discussed in Section 3.2 and can be found from the uncertainty in the intercept of the lines of best fit in Figure 13. The LOD is dependent on the relative intensity of lines within a spectra and the LOD is different for each element in a sample.

The resolution of our spectrometer was smaller than the FWHM of each studied line. It was not sufficient to use the highest measured value of a line on the spectrogram for our intensity measurements. The actual line peak was split between two pixels due to a finite instrumental resolution for most lines. In this thesis, a Voigt profile was fit to each line of interest within the spectrum to determine its amplitude, the surrounding thermal noise amplitude and the full-width half-max of the line. It was not always obvious if a given line was split between two pixels, so a Voigt profile was applied to every line for consistency. A Maxwellian distribution of velocities in the plasma contributed to spectroscopic line broadening in a Gaussian distribution while the collisions taking place in the plasma produce spectroscopic line broadening in a Lorentzian distribution. It is usually assumed that these two effects occur independently so it is appropriate to convolve the Gaussian and Lorentzian contributions into a Voigt distribution to model line broadening [24]. The fit profile was produced in Python using the LMFIT.MODELS package [35]. An example of the Voigt profile fitting is shown in Figure 14. The Voigt profile was produced using a closed-form approximation convolving the Gaussian and Lorentzian profiles. The program contained four variable parameters to input: a scaling amplitude factor A, the location of the line-centre μ, the covariance of the Gaussian profile σ, and the half-width half-max of the Lorentz profile γ.

$$F(x; A, \sigma, \gamma) = \frac{ARe[\omega(z)]}{\sigma\sqrt{2\pi}} \tag{56}$$

$$\omega(z) = e^{-z^2} erfc(-iz) \tag{57}$$

$$z = \frac{x - \mu + i\gamma}{\sigma\sqrt{2}} \tag{58}$$

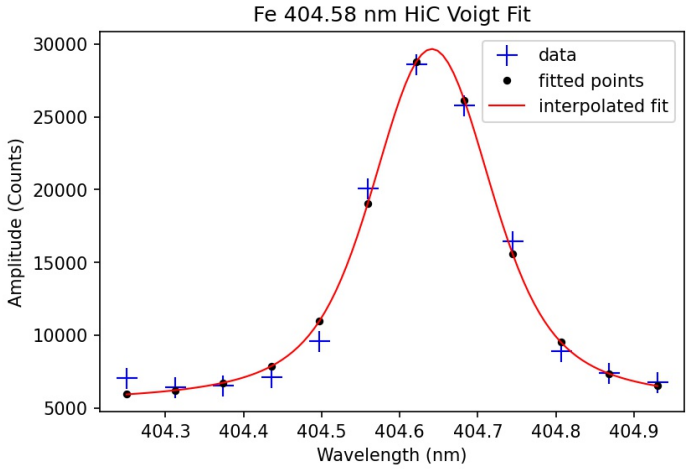

Figure 14: A Voigt profile (black dots, red line) is fit to the measured spectroscopic line (blue pluses) at 404.58 nm for CS HiC. The fitting finds the line peak at 404.64 ± 0.01 nm. The line amplitude is 24500 ± 1000 counts, the continuum is 5500 ± 500 counts, and the FWHM of the line is 0.18 nm.

The Olivero and Longbothum approximation was used to determine the FWHM of the fitted Voigt profile in LMFIT [36]. Using the final best-fit parameters for σ and γ, a weighted sum approximates the FWHM of the Voigt profile from the FWHM of both the Gaussian and Lorentzian fits. It can be shown [36] that

$$FWHM_{Gauss} = 2\sigma\sqrt{2ln(2)}, \qquad FWHM_{Lorentz} = 2\gamma$$

$$FWHM_{Voigt} = 1.0692\gamma + \sqrt{0.8664\gamma^2 + 5.545083\sigma^2} \tag{59}$$

Many different sets of σ and γ can produce a specific FWHM Voigt profile. By default, the LMFIT.MODELS package converges σ and γ to the same value based on the FWHM of the best-fit Voigt profile [35].

It is obvious from the shape of the fit in Figure 14 that the ions within the plasma

followed a Maxwellian velocity distribution and that electron-ion and ion-ion collisions occurred in the plasma. The good interpolated fit indicates that the Lorentzian and Gaussian broadening mechanisms acted independently and that the convolution of their profiles was an appropriate analytical method.

3.2 Self Absorption

Cool atoms at the edge of the plasma may absorb photon emission from the hot plasma center in a process called self-absorption. Self-absorption is typically visible in lines where the peak has a dip at the line center. In extreme cases, the curve of growth effect from optically thin media between the emitting sample and the spectrometer can split a line into two shallower lines. Self-absorption can also be seen as a non-linear dependency between emission intensity in high concentration samples [4]. Cool atoms self-absorb at a higher rate in samples with high elemental concentrations than in samples with low elemental concentrations. While no line splitting is visible in the spectra for the 520.84 nm Cr line, there appears to be self-absorption present in Cr I at concentrations above 15% because the intensity plot in Figure 13 (a) is non-linear. The line of best fit breaks from a linear dependency near 15% as shown in Figure 15. The spectral intensity increases at a reduced slope as the Cr concentration increases. The same non-linear dependency is not clear in the Fe I counts of Figure 13 (b). It should be noted that this non-linear effect could be due to the large uncertainties on chemical concentration given by the manufacturer. The plasma was optically thin, but not optically transparent to the emission wavelengths due to slef absorption.

The line of best fit parameters of the Cr I concentration plot in Figure 13 (a) are m = 1650 ± 150 counts/% and b = 2700 ± 1800 counts. The line of best fit parameters to the Fe I concentration plot are m = 90 ± 8 counts/% and b = 570 ± 620 counts. It is

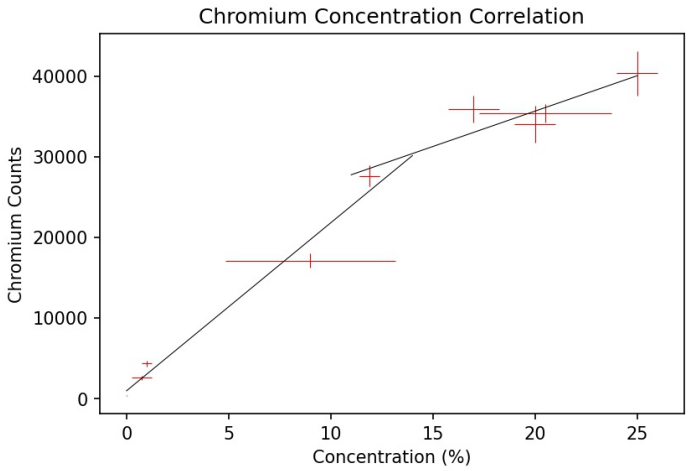

Figure 15: The effect of self absorption is approximated by two linear slopes that show the nonlinear dependency between intensity and concentration for the 520.8 nm Cr I spectral line.

logical to assume that both fits should have intercepts at zero counts. The Fe I concentration fit follows this assumption within uncertainty, however the Cr I concentration fit does not. The larger than expected intercept is not the result of a small sample size because a total of 135 data points from 27 different steel samples were used to produce the fit. Instead, this could be the result of self absorption in chromium suppressing the spectral line counts at high concentrations, which lowers the slope and raises the intercept of a straight line fit. Figure 15 highlights the evidence for self-absorption on Cr I spectral line intensity in the higher concentration samples of steel. Two separate lines of best fit are produced using intensity counts from the low concentration samples (CS4140, CSA2, CSAR500, CSHiC, SS410) and the high concentration samples (SS304, SS309, SS316, SS330, SS410). The low intensity line of best fit parameters are $m = 2090 \pm 180$ counts/% and $b = 960 \pm 1230$ counts. The high intensity line of best fit parameters are $m = 880 \pm 210$ counts/% and $b = 18000 \pm 4000$ counts. It is clear that the low intensity lines experienced minimal self-absorption and produced an

accurate line which intercepts the origin near zero counts at zero concentration. The high intensity spectral lines experienced self absorption at a greater rate and produced a much more inaccurate line of best fit due to the non-linear rate of line intensity suppression. The line of best fit produced using the high concentration spectral lines intercepts well above the origin, which is nonphysical. Due to the uncertainty in chemical composition provided by the manufacturer, it is not certain that self-absorption occurs in the steel. In a future study, calibrated samples with accurately known concentrations should be used to confirm the theory of self-absorption by Cr I in stainless steel samples.

The limit of detection (LOD) for Cr and Fe in our investigations with no time delay between the laser emission and the cooled camera is determined from the lines of best fit in Figures 13 (a) and (b). To find the LOD, take

$$\Delta y = m\Delta x + \Delta b \tag{60}$$

where Δy approaches zero when Δx approached the LOD. In other words, reliable, measurable counts approach zero at the LOD. Substituting Δx for the LOD, we can then write

$$|LOD| = \frac{\Delta b}{m} \tag{61}$$

where m is the slope and Δb is the uncertainty on the intercept from the line of best fit. Using these values from Figure 13 (a) and (b), $LOD_{Cr} = 1.1\%$ and $LOD_{Fe} = 6.9\%$. If the slope for low concentrations of Cr from Figure 15 is used, then $LOD_{Cr} = 0.6\%$. The difference between LOD_{Cr} and LOD_{Fe} is consistent with our data because the Cr I lines have a higher relative intensity than the Fe I lines.

3.3 Plasma Characterization

Production of Boltzmann plots are used to characterize properties of the plasma, such as its temperature, as outlined in Section 1.6.2. The characteristics determined from Boltzmann plotting apply only to the studied emitting species. In LTE, it is possible to determine the temperature of alloying elements such as chromium by producing the Boltzmann plot from spectrograms from chromium line emissions. No information about iron is in a Boltzmann plot produced by chromium lines.

The lines selected to plot the Boltzmann distributions followed a set of four rules [2, 37]. (1) There should be a large distribution of upper energy levels in the set of lines to minimize uncertainty in the statistical fit. (2) The spontaneous transition probability $A_{k,i}$ should be greater than 2.0×10^6 s^{-1} and should be known to a high precision for each line. Lines with a spontaneous transition rate lower than 2.0×10^6 s^{-1} emit at a rate on the order of the plasma de-excitation lifetime. (3) Avoid transitions involving low energy levels (ground states) because these tend to self-absorb. (4) The chosen lines must be isolated in the spectrum. 'Line blending' occurs when multiple emission lines overlap in the spectrum. Twelve Fe I lines and six Cr I lines were initially chosen to produce the set of Boltzmann plots and are listed in Table 3. All twelve of the selected Fe I lines were isolated with respect to other Fe emissions, however the Fe I line at 516.75 nm is blended with another line in the spectrum. Due to the line blending, the Fe I 516.75 nm line could not reliably be fit with a Voigt profile and was removed from consideration. The remaining lines (404-465 nm, 522-540 nm, 640, 649.5 nm) are produced from similar photon emission energies across de-excitation, however the selected lines have a good distribution of upper electron energy states (E_k) prior to emission which is a crucial condition for determining the characteristics of the plasma [25]. Elements with little initial electron energy state distribution are difficult

Table 3: The experimentally determined wavelength was found from the Voigt profile fitting procedure for all samples of steel and is shown below. The wavelength listed for each line in the NIST ADS database is shown in brackets. The upper and lower energies, level degeneracy and spontaneous transition probability of each line that was chosen to produce the Boltzmann distributions were retrieved from the NIST ADS Database.

Element	λ_{ki} (nm)	E_i (eV)	E_k (eV)	g_k	A_{ki} $s^{-1} \times 10^7$
Fe	404.64 ± 0.05 (404.58)	1.485	4.549	9	8.62
	406.43 ± 0.05 (406.36)	1.557	4.608	7	6.65
	413.31 ± 0.05 (413.21)	1.607	4.608	7	1.18
	418.31 ± 0.05 (418.17)	2.831	5.796	7	2.32
	423.69 ± 0.05 (423.59)	2.425	5.352	9	1.88
	522.68 ± 0.05 (522.72)	1.557	3.929	5	0.289
	526.83 ± 0.05 (526.95)	0.859	3.211	9	0.127
	532.73 ± 0.05 (532.80)	0.914	3.241	7	0.115
	538.18 ± 0.05 (538.34)	4.312	6.615	13	7.81
	639.87 ± 0.05 (640.00)	3.603	5.539	9	0.927
	649.22 ± 0.05 (649.49)	2.404	4.312	11	0.076
Cr	435.24 ± 0.05 (435.18)	1.030	3.878	11	1.2
	464.30 ± 0.05 (464.62)	1.030	3.698	7	0.87
	464.85 ± 0.05 (465.22)	1.004	3.668	5	0.58
	526.38 ± 0.05 (526.42)	0.968	3.323	3	0.41
	534.49 ± 0.05 (534.58)	1.004	3.322	5	0.49
	540.83 ± 0.05 (540.98)	1.030	3.321	7	0.62

to model accurately on a Boltzmann plot and provide larger systematic errors. Some Cr I lines, although intense in the spectrograms, face this issue. The six selected lines all have an upper electron energy state between 3 eV $< E_k <$ 4 eV. To contrast, the Fe I lines span 3 eV $< E_k <$ 6 eV. The lines for Fe at 526.9 nm, 532.8 nm and 649.5 nm do not meet the requirement in LIBS that $A_{ki} > 2 \times 10^6$ s^{-1}, however, this requirement is not strict. It will be shown later in this section that these three lines help produce a linear Boltzmann distribution.

Boltzmann plots of the Fe I lines were produced for the stainless steel samples in Figure 16 and for the carbon steel samples in Figure 17. Boltzmann plots of the

Cr I lines produced from the non-trace steel samples are shown in Figure 18. The vertical error bars in the plots represent statistical uncertainty from the Voigt fitting procedure. The data is composed of three trials for each sample. The mean amplitude from the three Voigt fitted profiles for each line is used to plot the Boltzmann distribution. A Boltzmann plot was produced for each sample of steel because it was assumed that each sample would produce slightly different plasma dynamics due to the varying chemical matrices between samples. The Saha-Boltzmann relationship given in section 1.6.2 can be linearized under the form y = mx + b by taking the natural logarithm on both sides of the Equation 27.

$$y = ln\left(\frac{I_{\lambda}^{ki}}{g_k A_{ki}}\right)$$

$$x = E_k$$

$$m = -\frac{1}{K_B T}$$

$$b = ln\left(\frac{FC_s}{U_s(T)}\right)$$

Boltzmann plots were produced by plotting the logarithm of the line intensity I_{λ}^{ki} (normalized to counts/s) against the upper electron energy state (E_k) for each mean spectroscopic line. The temperature of the iron species can be found by solving for the slope and the species number density can be found by rearranging the y-intercept equation as discussed previously in Section 1.6.2.

The presence of a linear Botlzmann distribution shows that the population of electronic states followed a Maxwellian exponential distribution across electron energy levels. The number of populated states decreased exponentially as the electron energy level increased. This exponential decrease corresponded to a linear relationship when

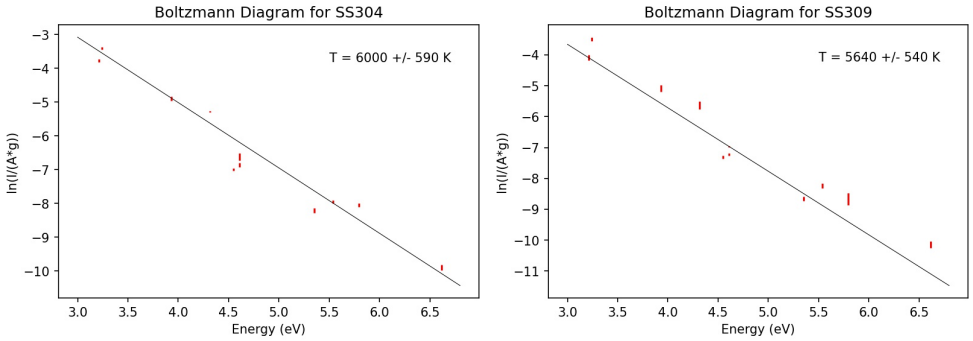

(a) The Boltzmann plot for SS 304.

(b) The Boltzmann plot for SS 309.

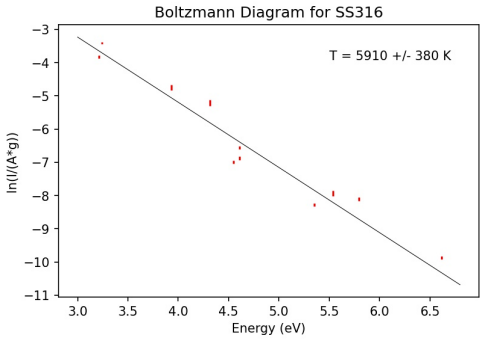

(c) The Boltzmann plot for SS 316.

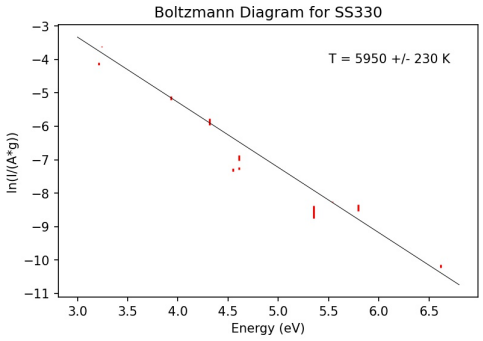

(d) The Boltzmann plot for SS 330.

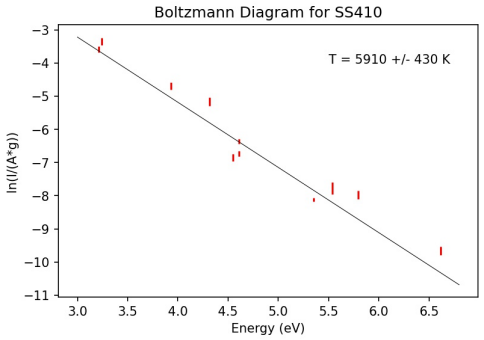

(e) The Boltzmann plot for SS 410.

Figure 16: The Boltzmann plots produced using the Fe I lines for the stainless steel samples. The black line is a linear fit to the red data points and is used to determine the temperature using Equation 30.

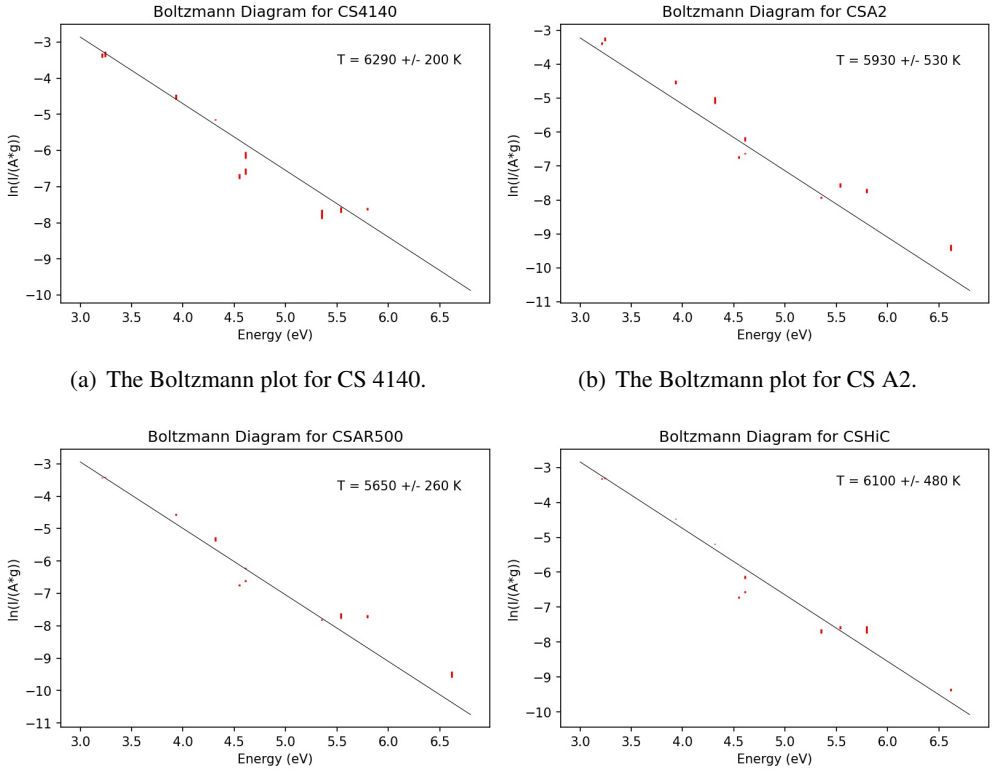

(a) The Boltzmann plot for CS 4140.

(b) The Boltzmann plot for CS A2.

(c) The Boltzmann plot for CS AR500.

(d) The Boltzmann plot for CS HiC.

Figure 17: The Boltzmann plots produced using the Fe I lines for the carbon steel samples. The black line is a linear fit to the red data points and is used to determine the temperature using Equation 30.

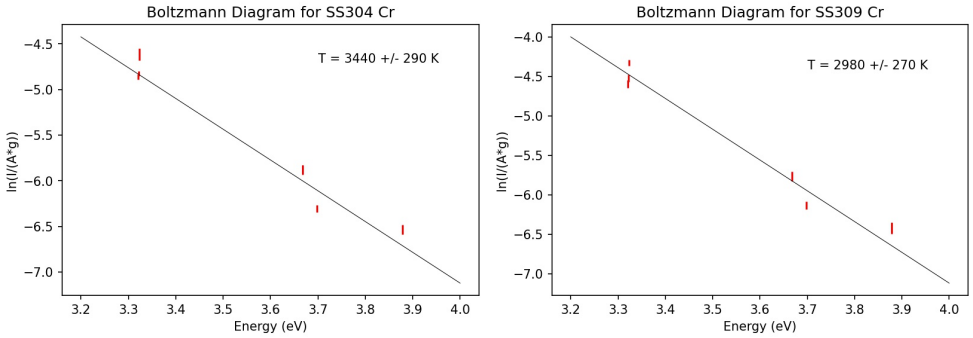

(a) The Boltzmann plot for SS 304.

(b) The Boltzmann plot for SS 309.

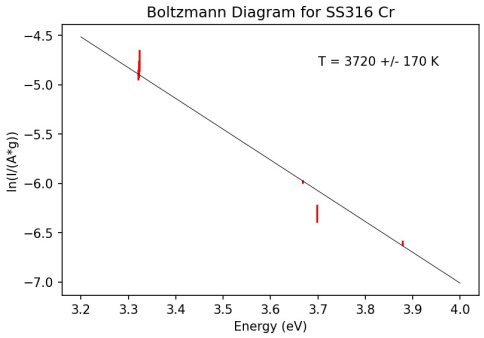

(c) The Boltzmann plot for SS 316.

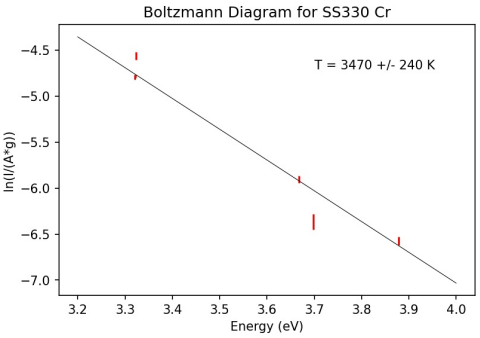

(d) The Boltzmann plot for SS 330.

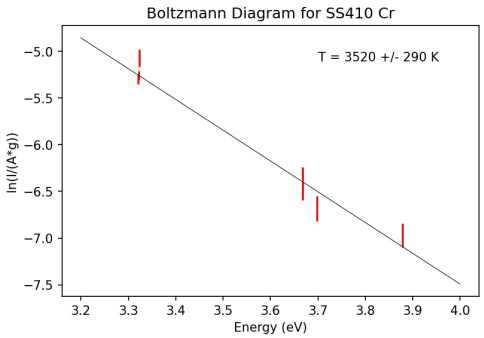

(e) The Boltzmann plot for SS 410.

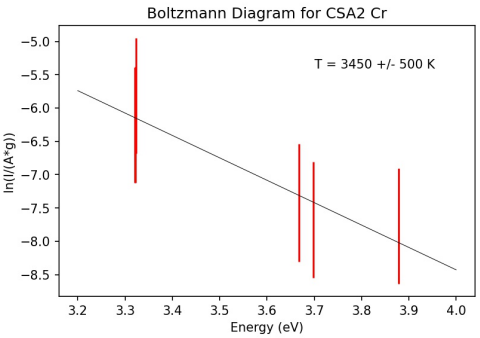

(f) The Boltzmann plot for CS A2.

Figure 18: The Boltzmann plots produced using the Cr I lines for the non-trace (Cr>1%) samples of steel. The black line is a linear fit to the red data points and is used to determine the temperature using Equation 30.

the logarithm of the Saha-Boltzmann relationship is taken. The linear Boltzmann plots are an indication that a given species, such as Fe I, in the plasma was in LTE but it is generally not a proof that the electrons and ions reached a thermodynamic equilibrium. Emission lines were visible in the spectra showing that the plasma was optically thin. An optically thin plasma is not a black body, such as a star, and internal radiation re-absorption occurs at a low rate which limits the heat transfer between different species. The Boltzmann plots produced different temperatures for the Cr I and Fe I species, a reasonable result given the low rate of radiative transfer within the plasma. The plasma was not able to reach a true local thermodynamic equilibrium due to the optical thinness of the plasma. The plasma appeared to be in a partial LTE state given the Maxwellian distribution of states in the plasma.

There are three main criteria that determine if the plasma is in an LTE state: the first criteria is to confirm that the electron number density (N_e) in the plasma is greater than the McWhirter and Hey limit, the second criteria is to confirm that the temperature and electron density rate of change in the plasma is small compared to the atomic excitation, and the third is to confirm that all species converge to a single temperature [38]. It is only possible to confirm the second criteria when using a Q-switch gating mechanism where the temperature and electron density can be measured at different gating delays to see how the values evolve over time. The third criteria was not held in this plasma, as shown by the Boltzmann plots. We must rely on satisfying the McWhirter and Hey criterion to indicate that the plasma reached a pLTE state. The McWhirter and Hey criterion is a necessary condition for LTE to exist in the plasma, but it is not a proof that the plasma is in LTE. Recall the McWhirter and Hey criterion [19],

Table 4: The approximate temperature of the Fe I ions as determined from the Fe I Boltzmann plots for each sample of steel. The electron density of the plasma for each steel sample was calculated using Equation 63. The Lorentzian Stark broadening FWHM was calculated from the Voigt profile fit to the 538.34 nm Fe I line for each sample of steel.

Steel	Temperature (K)	Electron Density (cm^{-3})	FWHM (nm)
SS 304	6000 ± 590	$7.6 \pm 0.2 \times 10^{16}$	0.18 ± 0.03
SS 309	5640 ± 540	$8.4 \pm 0.1 \times 10^{16}$	0.20 ± 0.01
SS 316	5910 ± 380	$8.3 \pm 0.4 \times 10^{16}$	0.20 ± 0.04
SS 330	5950 ± 230	$6.8 \pm 0.2 \times 10^{16}$	0.16 ± 0.03
SS 410	5910 ± 430	$7.3 \pm 0.1 \times 10^{16}$	0.18 ± 0.02
CS 4140	6290 ± 200	$8.2 \pm 0.1 \times 10^{16}$	0.20 ± 0.01
CS A2	5930 ± 530	$7.5 \pm 0.1 \times 10^{16}$	0.18 ± 0.01
CS AR500	5650 ± 260	$7.7 \pm 0.1 \times 10^{16}$	0.19 ± 0.01
CS HiC	6100 ± 480	$7.9 \pm 0.1 \times 10^{16}$	0.19 ± 0.02

$$N_e > 1.6 \times 10^{12} T^{\frac{1}{2}} (\Delta E)^3 \tag{62}$$

where T is the temperature of the plasma as determined from the Boltzmann plots and ΔE is the energy difference of electron states across emission (E_k - E_i). The highest energy photon studied should be used in solving the McWhirter criterion, which is the 404 nm Fe line (ΔE = 3.067 eV) in this case. It is then trivial to solve for N_e in Equation 62 to find the plasma must have $N_e > 3.7 \times 10^{15}$ cm^{-3}. A novel procedure has been developed to find the electron density in a plasma using the Fe 538.34 nm line [39]. Bengoechea et al. (2005) found a linear relationship between the total Lorentzian broadening of the linewidth and N_e in the range $4 \times 10^{16} < N_e < 15 \times 10^{16}$ cm^{-3} for the Fe I 538.34 nm line.

$$\omega_t = -0.011 + 2.56 \times 10^{-18} N_e \tag{63}$$

In Equation 63, ω_t is the FWHM from the Stark broadening of the Fe I 538.24 nm line

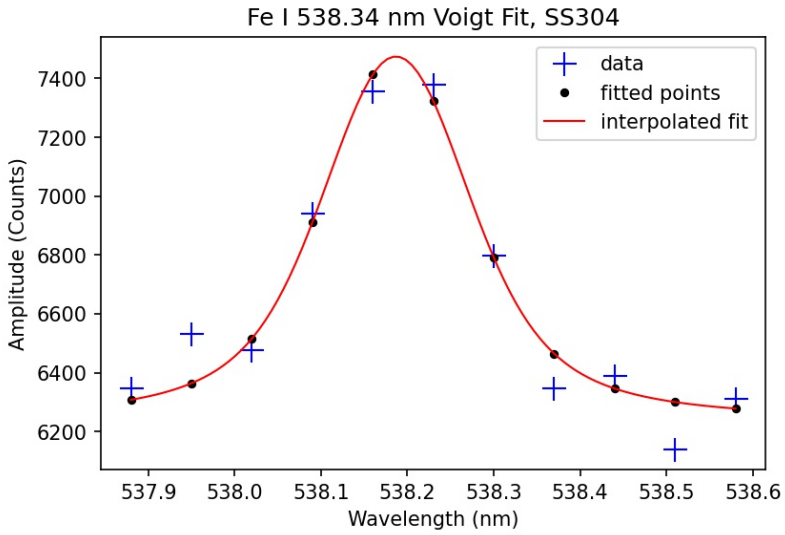

Figure 19: An example of the Voigt fit for the Fe I line at 538.24 nm is shown for the SS304 sample. The line amplitude was 1250 ± 125 counts, the noise amplitude was 350 ± 50 counts, and the FWHM of the line was 0.21 ± 0.02 nm. The FWHM of the Voigt fit was 0.18 ± 0.01 nm. A Stark shift at this electron density is typically -0.02 nm.

and N_e is the electron density in the plasma. The slope and y-intercept in Equation 22 were determined experimentally by the authors and have units of -0.011 nm and 2.56×10^{18} nm-cm^3, respectively [39]. Equation 63 was used to calculate the electron densities listed in Table 4. The FWHM of the Fe I 538.34 nm line was found by fitting a Voigt profile for each sample, as pictured in Figure 19. One key assumption in this thesis is that the Lorentz profile due to Stark broadening is the primary contribution to the Voigt profile width, which is a common assumption in the literature [19]. Natural lifetime broadening effects are Lorentzian and tend to broaden on the scale of 10^{-5} nm while broadening due to the Doppler effect from a Maxwellian distribution of moving particles is Gaussian and typically contributes broadening on the order of 10^{-2} nm for hot plasma near 10000 K [40]. Using Equation 24 confirms this: the spectroscopic line broadening due to the Doppler shift at a temperature near 6000 K is 0.022 nm. The sum of the non-Stark broadening is on the order of the systematic uncertainty of the FWHM produced from the Voigt profiles, therefore it is reasonable to use the Voigt profile FWHM as the Stark broadened FWHM for ω_t. Once ω_t was determined for each sample then it was possible to solve for N_e for all samples of steel reported in Table 4. All electron densities exceed the McWhirter criterion threshold and are within the required accuracy range for Equation 63 reported by Bengoechea et al. (2005).

4 Discussion & Future Works

4.1 Local Thermodynamic Equilibrium

For Local Thermodynamic Equilibrium (LTE) to exist in a plasma, a single temperature must be able to describe the electronic temperature (T_e) and the temperature of the excited ions (T_{exc}) in the plasma. Different temperatures were found for $T_{exc,Fe}$ and $T_{exc,Cr}$ from the Boltzmann plots, so LTE was not determined to exist in the laser induced plasma (LIP) for this investigation. The existence of linear Boltzmann distributions for the Fe I and Cr I ions do indicate LTE within the respective species, however the excited temperatures calculated from these plots do not agree within uncertainty with each other. The temperature of the electrons was not found because the excitation temperatures of Fe I and Cr I did not agree and calculating the partition function for Fe I was beyond the scope of this thesis. The Fe I ions reached a temperature near 6000 K while the Cr I ions reached 3500 K. The calculated electron density was above the McWhirter and Hey criterion threshold for both Fe and Cr. Some requirements for LTE are present, so we can say that a partial LTE was formed in the LIP as suggested by some authors [18]. We must be prudent in saying we did not reach full LTE because we could not confirm that T_e and T_{exc} converge to a single value without using a Q-switch gating mechanism for data acquisition. Although a partial LTE state was found in the plasma, a full LTE state is required to satisfy the Saha-Boltzmann relationship and to calculate the individual concentrations of each element in the matrix using the CF-LIBS approach. A comparison between the spectral counts and the concentration claimed by the manufacturer was produced to show the linear relationship between concentration and emission counts. Using steel samples with precise concentrations would be useful to calibrate Figures 13 and 15.

4.2 Scanning Electron Microscope Imaging

Assistance was provided by Dr. Jennifer Snelgrove of the Chemistry department at RMC to image the marks produced by the laser on the steel samples using a scanning electron microscope (SEM). The SEM was a Quanta 250 FEG Environmental Scanning Electron Microscope produced by the Field Electron and Ion Company and the operational settings are shown along the bottom of each image in Figure 20. A single spot irradiated by the laser on a SS316 steel sample is pictured in subfigures. The intense beam center ablated a hole in the steel and ejected material to create a crater. The ablated material emitted the light that produced the spectroscopic data, such as Figure 12. The beam intensity profile was Gaussian and weak near the edge of the beam. Beyond the ablation zone within the beam waist, steel melted from the heat of the resulting plasma and produced the ridges visible in Figure 20 (a) and (b). The spherical plasma expansion in open atmosphere caused the liquid steel to spread outward from the beam axis. As the plasma cooled between pulses, the liquid steel solidified and subsequent pulses added layers of re-solidified steel flakes onto the ridges. This effect is most visible in Figure 20 (a).

Circular patterns surround the crater in Figure 20 (b) where the laser is much weaker at large diameters (I = 0.1*I_0 at a 0.01 mm radius). The grains in the steel are bumpy and inhomogenous, and become smooth from the heat of the plasma beyond the laser beam. The grains of steel are visible in the fresh section of Figure 20 (c).

Figure 20 (a) supports the beam profiling results in Section 2.4 that claim the beam diameter is roughly 25 μm at the beam waist, ω_3. The scale shown on the bottom right of the image gives 50 μm as a reference width and the hole is roughly as wide as the reference. It is clear from the SEM images that the focal point ω_3 had a sufficient

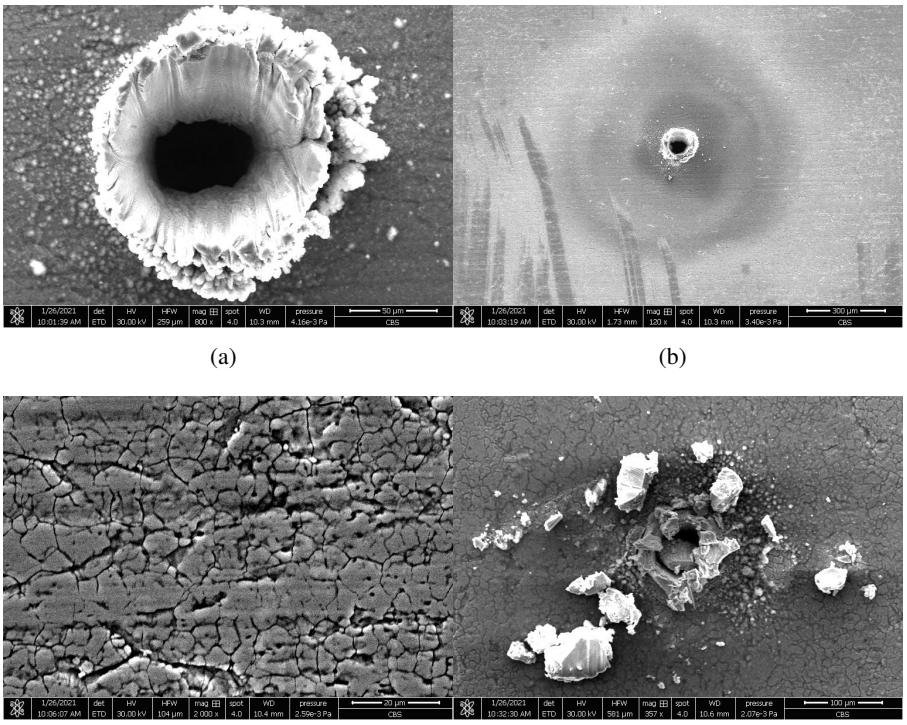

(a) (b)

(c) (d)

Figure 20: (a) A zoomed view and (b) a full view of the laser-ablated crater on a SS316 sample. (c) The grains within the steel sample of SS316. The image was taken on a fresh location away from the lased material. (d) A SS330 sample where the crater has crumbled.

intensity to ablate and vapourize the surface of the steel. This supports the Boltzmann plotting results that a high temperature was induced in a plasma. It was impossible to determine the depth of the hole using the SEM because the walls of the hole blocked electrons that entered from reaching the detector. The depth of the hole cannot easily be estimated by the remaining plume volume because an unknown amount of the steel completely ejected during ablation.

For the purposes of micro-machining, the intensity of the beam spot can be lowered to prevent rusting and minimize the ridges surrounding the crater. Suppose the

power of the laser is fixed, then the target can be moved beyond the beam waist to manually decrease the spot intensity while maintaining the fixed laser intensity. A picosecond laser could be used to minimize the thermal effects on the target or the beam can be swept across the target to minimize the creation of ridges. A spectrometer is useful to measure the spectral intensity of the plasma, where the line intensity within a spectrogram decreases as the spot intensity decreases. Boltzmann plots could quickly be produced to confirm that the plasma temperature decreases as the spot intensity decreases. By decreasing the laser spot intensity, it is possible to ablate steel without inducing rusting on the surface while micro-machining.

4.3 Modeling Rust growth in Fe-Heavy metals

As the plasma cooled, free Fe and O ions combined in the plasma to form rust molecules, namely iron Oxide (FeO), Ferrite (Fe_2O_3) and Magnetite (Fe_3O_4). On the surface of the steel, iron Oxide and Ferrite were visible as a light orange-red colour and Magnetite showed up as a dark brown-black colour. It appeared that Magnetite formed under a higher temperature (higher focal intensity) than Ferrite in the lab. More energy is required to ablate rust than steel because of rust's complex molecular structure; it behaves like an organic compound as discussed in Section 1.3.2. Rust growth on the surface of the steel slowed the flow of free Fe and Cr ions from the steel surface, hindering the plasma's sustainability. Measuring molecular lines from the rust de-excitation over time may correlate with the plasma intensity. A Magnetite line exists at 519.8 nm, however the amplitude is small and a time delay between the laser Q-switch and the cooled camera is recommended to resolve the line. iron Oxide, Ferrite and Magnetite have many emission lines near 600 nm, 480 nm and 520 nm, respectively. None of the iron oxide, ferrite or magnetite lines were resolved in this investigation and this is left

to future endeavors.

Work has been done to study how a laser removes rust from the surface of steel, and this is understood very well [41, 42]. Performing LIBS on a rusted piece of steel is similar to performing LIBS on clean steel, except a higher power density is required to break the complex molecular structure of rust. Rust behaves like an organic compound and requires photochemical ablation to excite a plasma, as is described in Section 1.3.2. De-rusting steel using LIBS ablates the rust layer off after a few laser pulses and the molecular lines can be seen in the spectra [41]. Once the rust is cleared, the laser begins ablating the steel surface and Fe I lines appear in the spectra. The number of pulses required for the Fe I lines to appear depends on the laser intensity at the beam waist and the pulse length.

From the work done in this thesis and in the lab, it was clear that rust formed sometime after or during the plasma de-excitation and it was clear the formed rust type (ferrite or magnetite) was dependent on the laser spot intensity. Beginning with the sample out of the focal point where plasma excitation still occurred, a mark with no rust was left on the steel. Moving the steel slightly more into the focal point caused an orange rust (ferrite) to appear on the steel. Then, right at the center of the focal point where the beam intensity was at a maximum, a black rust (magnetite) appeared on the marking after plasma de-excitation. Work has not been completed to model how quickly the rust forms after or during plasma de-excitation, or how the formed rust affects each subsequent laser pulse on the steel. There is a possibility to model the cyclical pattern of plasma excitation and rust production after plasma de-excitation in a pulsed LIBS system. It would be advantageous to use a time delay between the laser Q-switch and the cooled spectroscopic camera in such an investigation to observe when molecular rust de-excitaion lines begin to appear.

4.4 LIPS for Remote Sensing

Remote sensing is the acquisition of information from an object without making physical contact with the object. Taking an image of an object, such as a planet, using a spectrometer is an example of remote sensing. The methods outlined in this thesis are parallel to remote sensing in the idea that an image was taken of the plasma produced on the steel samples. This thesis, however, is an example of an in-situ experiment because the laser beam made contact with the sample to produce plasma. It is not technically possible to perform LIPS as remote sensing by its definition, but LIPS could be a valuable tool for remote sensing scientists in determining the chemical concentration of a given target.

Some obstacles exist for using LIPS as an aid for remote sensing that depend on the application. Focusing the laser over a large distance is a difficult restriction. Distances of a few meters pose little problem for focusing, but atmospheric thermal blooming effects and geometrical aberrations from a thick lens make it difficult to focus a beam to an accurate point across a few hundred meters. Over long distances, the laser must be increasingly powerful to induce a plasma due to the difficulties of focusing. The powerful laser heats the atmosphere, creating atmospheric thermal blooming that further refracts and distorts the laser beam. Atmospheric thermal blooming decreases the power density at the focal point by unevenly refracting the beam through dense regions of the atmosphere, lowering the power density at the laser focal point and slowing the plasma production. A time-delayed data acquisition is not feasible in a remote sensing application because it is impossible to know exactly how atmospheric blooming would affect plasma production. The light emitted from the plasma is also distorted by the atmosphere before entering the camera, altering the image of the plasma. Adaptive optics exist as a technique to resolve images taken by ground-based telescopes

where density variations in the atmosphere unevenly refract light and can be applied to remote LIPS spectra. Remote sensing targets are typically far away from the instruments, on the order of a few meters or up to a few hundred kilometers in the cases of satellite imaging. Q-switched time delay laser systems will not be compatible with these distances due to atmospheric perturbations along the beam path.

Typical objects of interest in remote sensing, such as glaciers and ecological habitats, may be studied using the pseudo in-situ process of calibrated LIPS in the field. This may happen either by visiting the object in person with a handheld LIPS system or by attaching a LIPS system to a remote controlled drone or a low-altitude airplane. LIPS may be used in mines to quickly and cheaply determine precious metal concentration in rocks. It has been used to study architecture and artwork from a short distance (~25 meters) [43]. LIPS can also be used in manufacturing plants to quickly determine the chemical concentration of a manufactured sample for quality control purposes.

5 Conclusion

This work has investigated the laser induced plasma (LIP) on pieces of common stainless and carbon steel, which included various concentrations of the alloying heavy metal chromium. The purpose of this work was to show that a LIPS system without a time-delay gating Q-switch could be used to determine the fundamental parameters of the induced plasma using the LIPS technique. A LIPS system that did not use a Q-switch to delay data acquisition was of interest in this thesis to show that LIPS is applicable to remote sensing projects that have a target sufficiently far away that thermal blooming from the atmosphere quantifiably alters the beam. Due to the uncertain time delay in plasma production from thermal blooming, typical Q-switch gating mechanisms are unreliable. In order to use the method without a time delay, it was necessary to test that the laser induced plasma was in a state of partial Local Thermodynamic Equilibrium (pLTE) so that LIPS could be used reliably. It was shown that various peaks of Fe I and Cr I were correlated with the elemental concentration though issues of self-absorption in high concentrations of Cr masked the results.

Boltzmann plots were produced from spectrograms for Fe I and Cr I species under the assumption of pLTE in the plasma, an assumption that was later supported by satisfying the McWhirter and Hey criterion. Each Boltzmann plot followed a linear relationship, indicating that the specie was in a pLTE state. However, in a system without a time delay for data acquisition, it was not possible to measure the dynamics of the plasma at specific time intervals so it was not possible to confirm that the electron temperature and the excitation temperatures of Fe I and Cr I converged to an equilibrium temperature. The Fe I ions were consistently near 6000 K and the Cr I ions were consistently near 3500 K at peak. The plasma was in a partial LTE state because the individual species showed evidence of LTE, but we could not represent all

species with a single temperature. The electron number densities in the plasmas were calculated using the Stark broadened FWHM for the Fe I line at 538 nm for each sample of steel. N_e was consistently around 7-8 $\times$ 10^{16} cm^{-3}, greater than the McWhiter and Hey criterion requirement of $N_e > 3.7 \times 10^{15}$ cm^{-3}.

Avoiding the use of a Q-switch to filter out the intense noise present in plasma formation makes it difficult to find trace elements in a sample. Using a Q-switch to delay data acquisition may be a requirement for future in-situ LIPS field measurements if the research relies on finding trace concentrations. It is unclear whether self-absorption in chromium affected the Boltzmann plots to suppress the temperature. A future study using samples with precisely known chemical concentrations can determine the role of self-absorption related to the Boltzmann plots. The plasma was in a partial LTE state, therefore it was not possible to reliably determine the chemical concentration of Cr and Fe within the samples using the CF-LIPS approach. It is possible to use the Calibrated LIPS approach to determine accurate chemical concentrations, though it is difficult to provide the necessary reference samples for research in the field. A Calibrated LIPS technique is likely limited to inorganic materials with a simple chemical matrix.

6 References

[1] M. S. Sankhla, M. Kumari, M. Nandan, R. Kumar, P. Agrawal, Heavy Metal Contamination in Water and their Hazardous Effect on Human Health-A Review. Int.J. Curr.Microbiol.App.Sci, (2016), 5(10): 759-766.

[2] G.S. Senesi, M. Dell'Aglio, R. Gaudiuso, Heavy Metal Concentrations in Soils as Determined by LIBS, with Special Emphasis on chromium. Environmental Research, 109 (2009), 413-420.

[3] G. Kim, J, Kwak, K. R. Kim, H. Lee, K. W. Kim, H. Yang, K Park, Rapid Detection of Soils Contaminated with Heavy Metals and Oils by Laser Induced Breakdown Spectroscopy. Journal of Hazardous Materials, 263, (2013), 754– 760.

[4] B. Sezer, G. Bilge, I. H. Boyaci, Capabilities and Limitations of LIBS in Food Analysis. Trends in Analytical Chemistry, 97 (2017), 345-353.

[5] G. Ji, P. Ye, Y. Shi, L. Yuan, X. Chen, M Yuan, D. Zhu, X. Chen, X. Hu, J. Jiang, Laser-Induced Breakdown Spectroscopy for Rapid Discrimination of Heavy-Metal-Contaminated Seafood Tegillarca granosa. Sensors. , 2017, Vol.17(11), p.2655.

[6] J. M. Anzano, I. B. Gornuskin, B. W. Smith, J. D. Winefordner, Laser-Induced Plasma Spectroscopy for Plastic Identification, Polymer Engineering and Science, 40 (11), (2000), 2423-2429.

[7] J. B. Sirven, B.Bousquet, L. Canioni, L. Sarger, S. Tellier, M. Potin-Gautier, I. Le Hecho, Qualitative and Quantitative Investigation of chromium-Polluted Soils by Laser-Induced Breakdown Spectroscopy Combined with Neural Networks Analysis, Anal. Bioanal. Chem. 385, 256-262, 2006.

[8] M. F. Spencer, Wave-optics investigation of turbulence thermal blooming interaction: II. Using time-dependent simulations, Opt.Eng. 59(8), 2020.

[9] X. Hou, B. T. Jones, Inductively Couple Plasma/Optical Emission Spectrom-

etry. Encyclopedia of Analytical Chemistry. R. A. Meyers (Ed), John Wiley & Sons Ltd. (2000), 9468-9485.

[10] J. C. Van Loon, Analytic Atomic Absorption Spectroscopy, Academic Press, (1980).

[11] L.J. Radziemski, D.A. Cremers, Laser Induced Plasmas, Marcel Dekker, New York, 1989.

[12] W. Lei, Temporal and Spatial Characteristics of Laser-Induced Plasma on Organic Materials and Quantitative Analysis of the Contained Inorganic Elements. Other [cond-mat.other]. Université Claude.

[13] J. Yu, Q. Ma, V. Motto-Ros, V. Motto-Ros, W. Lei, X. Wang, X. Bai, Generation and Expansion of Laser-Induced Plasma as a Spectroscopic Emission Source. Front. Phys. 7, 649–669 (2012).

[14] M. Yao, H. Yang, L. Huang, T. Chen, G. Rao, M. Liu, Detection of Heavy Metal Cd in Polluted Fresh Leafy Vegetables by Laser-Induced Breakdown Spectroscopy, Appl. Opt. 56, 4070-4075 (2017).

[15] M. Markiewicz-Keszycka, X. Cama-Moncunill, M. P. Casado-Gavalda, Y. Dixit, R. Cama-Moncunill, P. J. Cullen, C. Sullivan, Laser Induced Breakdown Spectroscopy (LIBS) For Food Analysis: A Review, Trends in Food Science & Technology, 65, (2017), 80-93.

[16] F. de Oliveira Borges, J. Uzuriaga Ospina, G. de Holanda Cavalcanti, E. E. Farias, A. A. Rocha, P. I. L. B. Ferreira, G. C. Gomes, A. Mello, CF-LIBS Analysis of Frozen Aqueous Solution Samples by Using a Standard Internal Reference and Correcting the Self-Absorption Effect, Journal of Analytical Atomic Spectroscopy, (2018), 33, 629-641.

[17] A. W. Miziolek, V. Palleschi, I. Schechter, (Eds), Laser-Induced Breakdown

Spectroscopy: Fundamentals and Applications, Cambridge University Press, 2006.

[18] G. Cristoforetti, A. de Giacomo, M. Dell'Aglio, S. Legnaioli, E. Tognoni, V. Palleschi, N. Omenetto, Local Thermodynamic Equilibrium in Laser-Induced Breakdown Spectroscopy: Beyond the McWhirter criterion, Spectrochimica Acta Part B: Atomic Spectroscopy, 65(1), 86-95, 2010.

[19] D. W. Hahn, N. Omenetto, Laser-Induced Breakdown Spectroscopy (LIBS), Part I: Review of Basic Diagnostics and Plasma-Particle Interactions: Still-Challenging Issues Within the Analytical Plasma Community, Appl. Spectrosc. 64(2010) 335A-366A.

[20] S. S. Harilal, C. V. Bindhu, R. C. Issac, V. P. N. Nampoori, C. P. G. Vanllabhan, Electron Density and Temperature Measurements in a Laser Produced Carbon Plasma. J. Appl. Phys. 82(5), (1997), 2140-2146.

[21] A. P. French, E. F. Taylor, An Introduction to Quantum Physics (1st Edition), Routledge, (1978).

[22] N. W. Ashcroft, N. D. Mermin, Solid State Physics, Saunders College, p. 8, Philadelphia, 1976.

[23] A. E. Siegman, Lasers, Mill Valley: University Science Book; p. 581-585, 1986.

[24] X. Huang, Y. L. Yung, A Common Misunderstanding About the Voigt Line Profile, Journal of the Atmospheric Sciences, Vol.61, (2004), 1630-1632.

[25] A. Ciucci, M. Corsi, V. Palleschi, S. Rastelli, A. Salvetti, E. Tognoni, New Procedure for Quantitative Elemental Analysis by Laser-Induced Breakdown Spectroscopy, Society for Applied Spectroscopy, 53 (8), (1999), 960-964.

[26] P. B. Johnson, R. W. Christy, Optical Constants of Transition Metals: Ti, V, Cr, Mn, Fe, Co, Ni, and Pd, Phys. Rev. 89, (1974), 5056-5070.

[27] A. Amran, N. K. Saat, Knife Edge Technique for Focused Beam Profiling of the Photothermal Imagin System, IOP Conf. Series: Journal of Physics: Conf. Series 1027, (2018).

[28] G. P. Beukema, Electrical Breakdown Properties of Stainless Steel and Titanium Electrodes in Ultra-High Vacuum. Physica B+C, 103(2-3), (1981), 397–411.

[29] J. S. Rigden, Macmillan Encyclopedia of Physics. Simon & Schuster, 1996: 353.

[30] C. Hönninger, R. Paschotta, F. Morier-Genound, M. Moser, U. Keller, Q-switching Stability Limits of Continuous-wave Passive Mode Locking, J. Opt. Soc. Am, (1999), 16, 46-56.

[31] U. Parali, X. Sheng, A. Minassian, G. Tawy, J. Sathian, G. M. Thomas, M. J. Damzen, Diode-Pumped Alexandrite Laser with Passive SESAM Q-Switching and Wavelength Tuneability, Optics Communications, 410, (2018), 970-976.

[32] L. Chen, Z. Gao, J. Ye, X. Cao, N. Xu, Q. Yuan, Construction Method through multiple Off Axis Parabolic Surfaces Expansion and Mixing to Design an Easy-Aligned Freeform Spectrometer, Optics Express, 27(18), (2019).

[33] Author unknown, Heat of Fusion and Vaporization, The University of Texas, GChem, https://gchem.cm.utexas.edu/data/section2.php?target=heat-transition.php, date unknown

[34] Author unknown, Heat Capacities for Some Select Substances, The University of Texas, https://gchem.cm.utexas.edu/data/section2.php?target=heat-capacities.php, date unknown

[35] M. Newville, T. Stensitzki, D. B. Allen, A. Ingargiola, (2014). LMFIT: Non-Linear Least-Square Minimization and Curve-Fitting for Python (0.8.0). Zenodo. https://doi.org/10.5281/zenodo.11813.

[36] J. J. Olivero, R. L. Longbothum, Emperical Fits to the Voigt Line Width: A Brief Review. Journal of Quantitative Spectroscopy and Radiative Transfer, Vol 17, 1977, 233-236

[37] Y. Zhang, Z. Zhao, T. Xu, G. H. Niu, Y. Liu, Y. Duan, Characterization of Local Thermodynamic Equilibrium in a Laser-Induced Aluminum Alloy Plasma, Applied Optics, 55 (10), (2016), 2741-2747.

[38] E. Tognoni, G. Christoforetti, S. Legnaioli, V. Palleschi, Calibration-Free Laser-Induced Breakdown Spectroscopy: State of the Art, Spectrochimica Acta Part B, 65, (2010), 1-14.

[39] J. Bengoechea, C. Aragon, J. A. Aguilera, Asymmetric Stark Broadening of the Fe I 538.34 nm Emission Line in a Laser Induced Plasma, Spectrochimica Acta Part B, 60, (2005), 897-904.

[40] S. Zielinska, S. Pellerin, K. Dzierzega, F. Valensi, K. Musiol, F. Briand, Measurement of Atomic Stark Parameters of Many Mn I and Fe I Spectral Lines Using GMAW Process. Journal of Physics D: Applied Physics, IOP Publishing, (2010), 43 (43), pp.434005. 10.1088/0022-3727/43/43/434005. hal-00569734.

[41] O. Ogboghodo, Laser Induced Breakdown Spectroscopy for Identification & Quantification of Elemental Composition of Steel Structures: A Study of Early Stage Rust Behaviour in Steel, International Journal of Scientific and Research Publications, 5 (5), (2015), 797-808.

[42] R. Zha, Y. Bai, L. Yu, B. Li, J. Zhou, Laser Derusting on Low Carbon Steel Surface Based on Coordinated Application of Machine Vision and Laser-Induced Breakdown Spectroscopy, Appl. Opt. 61, 2147-2154 (2022).

[43] F. J. Fortes, J. Cuñat, L. M. Cabalín, J. J. Laserna, In Situ Analytical Assessment and Chemical Imaging of Historical Buildings Using a Man-Portable Laser System, Appl. Spectrosc. 61, (2007), 558.